PHYSICAL REVIEW E VOLUME 56, NUMBER 4 OCTOBER 1997

Onset of relativistic self-focusing in high density gas jet targets

R. Fedosejevs,* X. F. Wang,† and G. D. Tsakiris
Max-Planck-Institut für Quantenoptik, Hans-Kopfermann Strasse 1, D-85748 Garching, Germany

(Received 20 May 1997)

Optical investigations are reported of the interaction of 0.3 TW, 250 fs Ti:sapphire laser pulses with underdense plasmas created from high density gas jet targets. Time resolved shadowgraphy using a 2ω probe pulse, images of the transmitted radiation and images of 1ω and 2ω side radiation are presented for various gases. The experimental results and their analysis based on a simple numerical Gaussian beam model show that ionization-induced refraction dominates the interaction process for all gases except hydrogen. The numerical modeling also shows that for a given laser power there exists only a narrow density range in which self-focusing can be expected to occur. In the case of hydrogen for electron densities greater than $\sim 10^{20}$ cm^{-3}, the onset of channeling expected at the critical power for relativistic self-focusing is experimentally observed. X-ray and forward stimulated Raman scattering measurements were also conducted to verify the onset of high intensity relativistic interactions and the onset of fast electron generation. [S1063-651X(97)11709-3]

PACS number(s): 52.40.Nk, 42.65.Jx, 52.35.Mw, 52.40.Db

I. INTRODUCTION

The intensities now achievable with high power femtosecond laser systems can approach 10^{18}–10^{19} W cm^{-2} for which the interaction of the laser pulse with plasma becomes relativistic in nature. The propagation of such ultrashort high intensity laser pulses in underdense plasma is of interest both for the understanding of laser interactions in this new relativistically driven plasma regime and for applications such as laser wake field accelerators [1–3], x-ray lasers [4–7], and the fast ignitor concept for inertial confinement fusion energy [8]. For many of these applications long interaction lengths of several times the diffraction limited Rayleigh length are either desirable or necessary. In order to obtain such long interaction lengths some mechanism must be invoked in order to compete with the normal diffraction of light. For terawatt laser pulses the relativistic nature of the interaction can result in relativistic self-focusing of the radiation [9–11] which, in turn, may naturally lead to long interaction lengths.

At high intensities two factors contribute to this focusing on a femtosecond time scale. The first is the relativistic mass increase of the oscillating electrons leading to a decrease in the plasma frequency and thus a local increase in the refractive index. The second is the ponderomotive expulsion of electrons from the beam path such that the ponderomotive force is balanced by the electrostatic field set up between the displaced electrons and the ions that remain on axis. These factors lead to a positive focusing effect that becomes stronger as the laser beam decreases in diameter and becomes more intense. The end result is a self-focused channel with a radius of the order of the plasma skin depth with the complete expulsion of the electrons from the plasma channel. Propagation over several Rayleigh lengths has already been demonstrated [12–14] at relatively low densities in the range of $(0.01-0.03)n_c$, where $n_c = m\omega_L^2/4\pi e^2$ is the critical electron density and ω_L the laser frequency. The threshold power for such relativistic self-focusing is given by $P_c = 16.2 n_c/n_e$[GW] where n_e is the electron density. Thus, in order to achieve self-focusing at modest power levels it would be advantageous to operate at higher values of electron density of the order of $0.1n_c$ or more. At very high intensities additional factors such as self-generated magnetic fields and acceleration of fast electrons [15] may come into play to further stabilize or modify the self-focusing process.

Gas targets provide one of the simplest forms of underdense media. However, if a simple gas target is used, the self-focusing process must compete with the refraction of the pulse from the self-generated electron density profile due to the ionization of the gas. The predominant mechanism for ionization is tunnel ionization [16,17] whose rate climbs dramatically once the laser field approaches the electric field holding the outermost electron in place. In many cases the ionization can be considered to be instantaneous once this Coulomb potential barrier has been exceeded, yielding intensity thresholds for the formation of each ionization stage of an atom [18]. Since laser beams typically have a high intensity on axis and low intensity at the edge of the beam, the result is an ionization profile that has high ionization in the center of the propagation path and low ionization at the edge. This in turn leads to refraction of the laser light away from the axis. This limitation has been considered theoretically [5,19–21] and demonstrated experimentally [22–24]. Thus in order to achieve long propagation lengths the self-focusing mechanism must be strong enough to overcome not only the normal diffraction but also the ionization induced refraction. This competition becomes more severe at higher plasma densities since the refraction effect scales with density. A reduction of the refractive defocusing can be obtained by employing a gas jet target instead of a uniform background gas. In this case the refraction over the long path length prior to the interaction region can be eliminated. However, as will be seen from the results presented here the refraction in the main interaction region of interest is still

---

*On leave from the Department of Electrical Engineering, University of Alberta, Edmonton, Canada.

†On leave from the Shanghai Institute of Optics and Fine Mechanics, Chinese Academy of Sciences, Shanghai, China.

very strong and can significantly limit the achievable peak intensities.

In order to eliminate the ionization refraction and allow propagation over several Rayleigh lengths it has also been proposed that a preshaped low density channel with high density walls be employed. When ionized, this channel will have a lower electron density in the center than at the walls and will result in the guiding of the radiation within the channel [5,24]. The guiding effect of such a channel has recently been demonstrated by Durfee and Milchberg [25]. However, the creation of such a guiding channel requires a second laser pulse and a suitable optical illumination system, which may not be feasible in many experiments.

It is thus useful to explore in what regimes the relativistic self-focusing itself might lead to guiding of the radiation. Previous experiments using gas targets have only demonstrated relativistic self-focusing at relatively low densities in the range $(0.01-0.03)n_c$ [12–14]. More recent experiments [26,27] have demonstrated the effects of relativistic self-focusing in preformed plasmas at higher electron densities of over $0.1n_c$ but these experiments have used fully preionized exploding foil targets. However, no experiments have explored the limits of relativistic self-focusing at high interaction densities in simple gas targets where the refractive defocusing would be strong.

A further complication in the interaction of lasers at such high intensities is the onset of stimulated Raman scattering (SRS) in the backward and forward directions. If strongly driven, these processes can lead to the generation of fast electrons by wave breaking and the eventual self-modulation of the propagating laser pulse. Observations of Raman scattering for short pulse high intensity interactions have been reported in a number of experiments [22,28,29] for both gas jet and static fill gas targets. The effects of self-modulation of the laser pulse and potential enhancement of wake field generation for electron accelerators have also been predicted in a number of reports [3,31]. The characteristics of the Raman spectra can serve as a useful diagnostic of electron density or, if the background density is known, the electron temperature of the interaction region. Also, if significant refractive defocusing occurs, the decrease in Raman signal with gas density is indicative of the threshold where such refraction becomes dominant.

In the high intensity regime a number of processes can lead to the generation of fast electrons. The relativistic self-focusing itself can generate electrons with energies of the order of MeV [15] while the acceleration by the plasma wake field behind the laser pulse can also generate electrons of a similar energy [14,31]. The stimulated Raman scattering process itself will generate fast electrons by the damping and breaking of the plasma waves generating electrons with an energy approximately given by a few times the phase velocity of the plasma waves [30,31]. In the case of forward Raman scattering for which the wave vector is small this typically is in the range of MeV while for the backward process where the wave vector is larger it is of the order of 10 keV. Thus, electrons are also a useful diagnostic of the high field interaction process.

In the present paper we explore the competition between the three processes of diffraction, ionization-induced refraction, and relativistic self-focusing for relatively high interaction densities on the order of $0.1n_c$ in both uniform gas targets and gas jet targets. A theoretical analysis is carried out based on a Gaussian beam propagation model and used to define various regions for which self-focusing or refraction should dominate. Experimental measurements are carried out in order to verify these predictions primarily for gas jet targets. Different gases including hydrogen, helium, nitrogen, neon, argon, and xenon were investigated in order to observe the dependency on ionization-induced refractive effects. A variety of diagnostics were used including shadowgraphy, imaging of the transmitted radiation, and self-emission at the fundamental and second harmonic wavelengths. In addition, measurements were made of backscattered and forward scattered stimulated Raman radiation and hard x-ray radiation in order to verify when the interactions were approaching the relativistic regime.

II. EXPERIMENTAL SETUP

The experiments were carried out using a terawatt Ti:sapphire laser system that delivered 80 mJ, 250 fs pulses at 790 nm to a gas jet target. The radiation was focused using a 90° 14 cm focal length, $F_{\#}=2.5$ off-axis parabola. The parabola was made of copper which was electroplated with nickel, diamond turned and hand polished to remove most of the tool marks. The beam path from the output of the grating compressor to the interaction target chamber was evacuated. However, the air path in the compressor system combined with the path length through the entrance windows led to a significant B integral, which in turn led to some degradation of the beam quality at the target. The final beam quality on target was diffraction limited several times primarily limited by the quality of the compressor optical components, the B integral, and scattered radiation from the parabola surface. The off-axis parabola was aligned using a charge-coupled device (CCD) imaging system, which viewed a magnified image of the focal spot. The orientation of the parabola was adjusted to give the maximum brightness focal spot leading to highest interaction intensity at focus. Images were taken of the radiation intensity at various positions in front of and behind the point of best focus. The vacuum focal spot had a peak intensity of 3×10^{17} W/cm^2 in a central spot of 5 μm diameter and a 50% energy containing diameter of 20 μm. Because the beam was several times the diffraction limit the beam had hot spot regions on front of and past the best focus position and the length of region between the 50% intensity points was $\sim$130 μm.

The pulse duration was measured using a second-order single-shot autocorrelator with a dynamic range of over 10^3. Early prepulses occurring on a nanosecond time scale prior to the main pulse were suppressed by 5 orders of magnitude so that they did not lead to premature breakdown of the gas target. Prepulses occurring in the range of picoseconds prior to the main pulses were also suppressed by more than 3–4 orders of magnitude.

The detailed experimental layout is shown in Fig. 1. The 50 mm diameter laser beam was incident through a 3 mm thick quartz window into the interaction chamber, which was evacuated below 10^{-3} mbar background pressure prior to each laser shot. Before the target chamber a beam splitter consisting of a 520 μm thick quartz wafer that was antire-

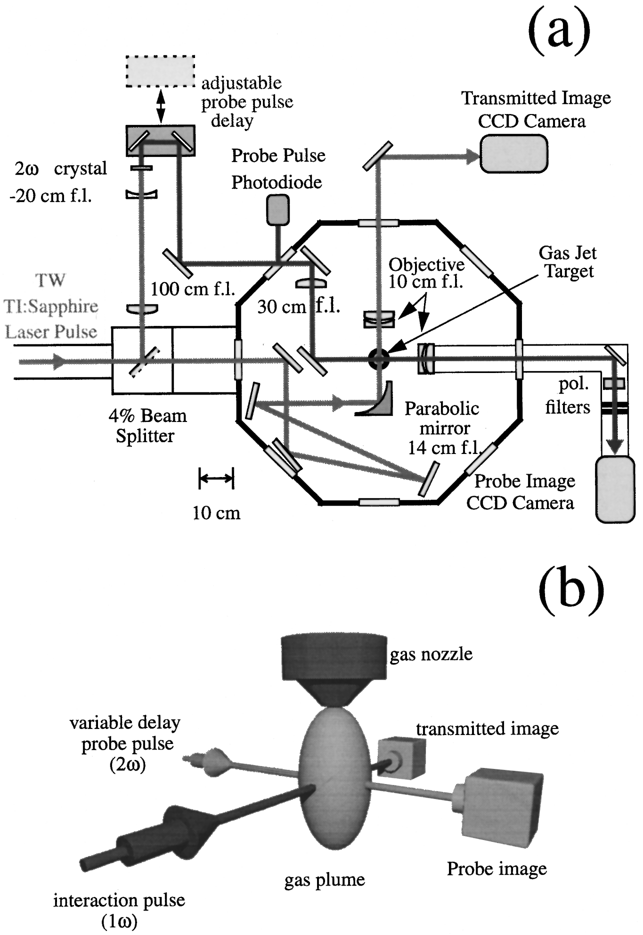

FIG. 1. (a) Schematic of the experimental setup. (b) Perspective view of the gas jet and interaction region geometry.

flection coated on one surface was used to separate out 4% of the main beam. This pulse was reduced in diameter 5 times to 1 cm in diameter, frequency doubled in a 2 mm thick KDP crystal, and reflected through a variable optical delay line in order to give a second harmonic probe pulse adjustable in time relative to the main pulse. A 30 cm focal length lens was used to give a small 500 μm diameter probe spot through the interaction region at 90° relative to the main beam. The near field distribution of the laser pulse was strongly modulated leading to enhanced intensity nonuniformity in the second harmonic probe beam. In addition, at times, the probe beam would be apertured by one or more of the optical components leading to diffraction fringes in the spatial profile.

Three different optical diagnostic measurements were carried out including: (1) time resolved shadowgraphy, (2) self-scattered time integrated images of 1ω radiation at 90° to the main beam direction, and (3) 2ω time integrated images of the plasma. In all three cases the interaction region was imaged onto a CCD camera with a magnification factor of 8 times using a high resolution multiple element $F_{\#}=2.5$, 10 cm focal length objective. The effective resolution of the imaging system was of the order of 3 μm. Various calcite or thin film polarizers could be introduced into the imaging system in order to analyze the polarization of the detected radiation. For self-emission at the fundamental wavelength an interference filter centered at 790 nm with a bandwidth of 13 nm was introduced into the imaging system. For shadowgraphy and for 2ω imaging a filter centered at 400 nm with a 33 nm bandwidth was employed.

A similar imaging system was employed to view the laser radiation transmitted through the interaction region. In order to reduce the intensity and minimize any distortion of the beam through additional self-focusing in the imaging system elements, a 25% transmission neutral density filter and a 1% transmission dielectric mirror were used as the first two optical elements in the imaging system. This was followed by several decades of optical filters before the CCD camera. In a number of cases the imaging system was adjusted to image the plane 250 μm past the position of best focus in order to measure the degree of spatial deflection of the beam passing through the interaction region.

Measurements were also carried out of the transmitted and backscattered spectra in search of Raman forward and backscattered radiation. For measurements of the transmitted spectrum a fiber optic coupler was positioned to intercept the central part of the transmitted radiation as imaged by the transmitted light imaging system. The radiation picked up by the fiber was directed into a low resolution diode array spectrometer. The spectrometer [32] had a spectral resolution of 3.3 nm in the range of 300–1130 nm. For the forward scatter, an equivalent collecting optical aperture of $F_{\#}=57$ was sampled in the exact forward direction. The backscattered radiation was measured by the same spectrometer on a different set of shots. In this case the backscattered radiation was intercepted by a 3 mm thick quartz beam splitter, which was placed before the parabolic focusing mirror. In order to calibrate the absolute reflectivity level for the backscattered diagnostic, an uncoated glass plate was inserted after the beam splitter in order to retroreflect 8% of the incident radiation into the diagnostic channel. The transmitted radiation channel was calibrated for 100% transmission by taking shots with no gas target present.

A simple circular orifice free expansion gas jet with a diameter of 500 μm was employed for these experiments. The jet was identical to that characterized by Li and Fedosejevs [33] except that the outlet diameter was 500 μm instead of 1000 μm. The gas density profile of the current gas jet was measured interferometrically for the different gases used in the present experiment including, hydrogen, helium, neon, and nitrogen. The density profiles at a distance of 200–400 μm from the nozzle outlet could be adequately characterized by a simple Gaussian radial profile and an exponential density falloff with distance from the nozzle orifice. The accuracy of the density measurements was estimated to be $\pm 25\%$. For nitrogen gas at a reservoir backing pressure of 10 bar a peak density of 5.4×10^{19} atoms per cm^3 was obtained at a distance of 300 μm from the nozzle exit, which if ionized to 5^+ ionization state (as expected from tunnel ionization for intensities of 5×10^{16} W/cm^2) would lead to an electron density of $n_e/n_c=0.15$.

Recent experiments [34,35] have studied the interaction of high intensity laser pulses with gas clusters indicating enhanced absorption and x-ray emission. Using the standard model for the expansion, cooling and cluster formation in gas jets [36] we find that we are in the near field range of the gas orifice, i.e., within one nozzle diameter of the exit, and thus sufficient cooling of our gas does not occur for the formation of clusters in the gases that we have used in our experiments. Thus the following reported interactions are between the incident laser pulse and a homogeneous atomic or molecular gas target.

Filtered x-ray-scintillator photomultiplier detectors were used to detect hard x-ray emission from the laser-gas interactions. A 150–550 μm thick aluminum foil was set before the scintillator to attenuate soft x rays, UV and visible light, which means that the scintillator would detect x rays with photon energy greater than 8 keV with the 150 μm Al filter and 12 keV with the 550 μm Al filter. The plastic scintillator was 16 mm thick which meant that higher energy x rays significantly above 20 keV would be partially transmitted. The signal from the scintillator was detected by a photomultiplier that was read out by connecting it to a storage oscilloscope.

III. THE RAY TRACING MODEL

Understanding the way in which short ($\lesssim 1$ ps) intense ($\gtrsim 10^{15}$ W/cm^2) laser pulses interact with relatively dense gases requires the detailed investigation of all processes that affect the spatial beam profile during propagation. At these intensities the medium undergoes rapid ionization right at the leading edge of the pulse so that the subsequent interaction is that of an intense pulse with an underdense plasma. The number of electrons that are produced via ionization at a particular point of the beam path strongly depends on the prevailing local intensity. As a consequence, any intensity variation across the beam profile would give rise to a spatially varying index of refraction, which in turn would alter the propagation of the individual rays through the medium, thus further modifying the beam path. A Gaussian-like radial intensity profile would produce via ionization an excess of electrons around the beam axis, which would lead to defocusing because of the lensing effect associated with such a density profile. In addition the diffraction of the beam leads to a defocusing affect independent of density. A counteracting process is the relativistically induced self-focusing due to the electron mass increase in high intensity regions and the expulsion of electrons from these regions by the ponderomotive force.

In the limit where the laser pulse contains many laser oscillations, the refractive index of the plasma η is given by [9,37–39]

$$\eta = 1 - \frac{1}{2}\frac{\omega_p^2}{\omega_L^2}\frac{1}{(1+a_L^2/2)^{1/2}}, \tag{3.1}$$

where $\omega_p = (4\pi e^2 n_e/m)^{1/2}$ is the plasma frequency, ω_L is the laser frequency, and $a_L = eA_L/mc^2$ the amplitude of the normalized vector potential, which in terms of the peak electric field is given by $A_L = cE_L/\omega_L$.

For intensities pertaining to the experimental conditions (see Sec. II), i.e., for mildly relativistic intensities ($a_L^2 \lesssim 1.0$), the expression in Eq. (3.1) can be simplified to read

$$\eta \approx 1 - \frac{1}{2}\frac{\omega_p^2}{\omega_L^2} + \frac{1}{8}\frac{\omega_p^2}{\omega_L^2}a_L^2. \tag{3.2}$$

The last term in Eq. (3.2) is easily recognized as due to the relativistic effects since for $a_L^2 \approx 0.0$ it disappears. As is seen from the analysis that follows, the second term gives rise to refractive defocusing. It should be pointed out here that although the expression in Eq. (3.2) includes self-focusing associated with the relativistic intensities and the ponderomotive electron expulsion from the high intensity regions, it does not include effects such as electron cavitation [11]. Given that $\omega_p^2 \sim n_e$, one concludes that the ionization of the medium affects not only the refractive, but also the relativistic self-focusing term.

A. The paraxial ray equation

The problem of beam propagation in a medium undergoing ionization at relativistic intensities can be treated using the paraxial ray equation for a Gaussian beam [40,41,21]

$$\frac{d^2 r}{dz^2} = \frac{1}{\eta_0}\frac{\partial \eta}{\partial r} + \frac{\lambda^2}{4\pi^2}\frac{r}{r_0^4}. \tag{3.3}$$

We use here the same formulation and notation as in Ref. [21]; i.e., $r(z)$ gives the variation of the radius of a particular ray along the beam axis. The first term in the right side of Eq. (3.3) represents the contributions from the refraction index gradient, which is assumed to vary quadratically with distance r from the axis, i.e.,

$$\eta(r,z) = \eta_0 - \tfrac{1}{2}\eta_2 r^2. \tag{3.4}$$

The last term in Eq. (3.3) describes the diffraction of a Gaussian beam with an intensity variation given by

$$I(r,z) = I_0 \exp\left(-\frac{r^2}{r_0^2}\right). \tag{3.5}$$

Keeping in accordance with Ref. [21], the radius of the beam is defined here as $r_0(z) = w_0(z)/\sqrt{2}$ where $w_0(z)$ is the customary beam waist. This means that the intensity at the beam center is related to the total beam power P through $I_0 = P/(\pi r_0^2)$.

Equation (3.3) consistently describes the propagation of a Gaussian beam as long as the index of refraction exhibits the r dependence implied by Eq. (3.4). In Ref. [21] it was shown that for the case of ionization induced refraction the plasma index of refraction $\eta = 1 - \omega_p^2/(2\omega_L^2)$ can be put in the form of Eq. (3.4). In what follows this formalism is extended to include relativistic self-focusing using the complete expression for η as given by Eq. (3.2).

1. The paraxial ray equation in a fully ionized plasma

In the case of high intensities and low Z gases, the medium ionizes completely so that the pulse propagates through a homogeneous plasma of constant electron density. Under these circumstances, there are no contributions from the second term in Eq. (3.2) and the refractive index gradient is $\partial\eta/\partial r = (\omega_p^2/8\omega_L^2)\partial a_L^2/\partial r$.

Using the relation $a_L^2 = (2r_e/\pi mc^3)\lambda^2 I$ between normalized vector potential and intensity (here $r_e = e^2/mc^2$ denotes the classical electron radius) and the definition of the critical power for self-focusing $P_c=(2mc^3/r_e)(\omega_L/\omega_p)^2$ (see, e.g., [10]) the last term in Eq. (3.2) can be written as $(\lambda^2/2\pi^2 r_0^2)(P/P_c)\exp(-r^2/r_0^2)$. Accordingly, the refractive index gradient is then given by $\partial\eta/\partial r=-(\lambda^2/\pi^2 r_0^4)(P/P_c)r/e$. Here we have used the approximation $[\partial e^{-r^2/r_0^2}/\partial r]_{r\approx r0}\approx -2r/(er_0^2)$, which means that the refractive index gradient is evaluated near the radial position $r\approx r_0$. This is to best evaluate the overall beam evolution, which is adequately described by following the ray path at a distance $r=r_0$ from the propagation axis. Introducing these results into Eq. (3.4) and for $\eta_0\approx 1$ one obtains the paraxial ray equation for fully ionized plasma in the form

$$\frac{d^2r}{dz^2}=\frac{\lambda^2}{4\pi^2 r_0^4}\left(1-\kappa\frac{P}{P_c}\right)r. \tag{3.6}$$

This is the well known [41,42] Gaussian beam ray equation for self-focusing in a medium with index of refraction possessing a term linearly dependent on intensity. Here $\kappa=4/e=1.47$ denotes a factor dependent on the position of the ray considered, which we call the *position factor*. The solution of Eq. (3.6) gives the variation of the beam radius with z in the form $r^2(z)=r_{0,\min}^2[1+(1-\kappa P/P_c)(z/z_{0,\min})^2]$ with $z_{0,\min}=2\pi r_{0,\min}^2/\lambda$, which leads to a minimum beam radius of $r_{0,\min}$ in the case $P<P_c/\kappa$ or to whole beam focusing for $P>P_c/\kappa$.

2. The paraxial ray equation in an ionizing plasma

When the ionization process is taken into account, the explicit dependence of the electron density on the intensity has to be introduced in the expression for the index of refraction in Eq. (3.2). In this case, the terms containing a factor proportional to ω_p^2 give rise to additional intensity dependent terms.

According to the Coulomb-barrier ionization model, the charge distribution across the beam can be approximated as a continuous function of intensity and is given by [21]

$$q(r,z)=q_0 I(r,z)^{1/(4\alpha-2)}. \tag{3.7}$$

The constants q_0 and α are determined from the ionization potentials for the different gases (see Sec. III A 3). Introducing the Gaussian beam intensity profile from Eq. (3.5) in Eq. (3.7) and using the relation $\omega_p^2/\omega_L^2=qn_a/n_c$ where n_a is the atomic gas density one obtains

$$\frac{\omega_p^2}{\omega_L^2}=\frac{q_0 n_a}{n_c}\left(\frac{P}{\pi r_0^2}\right)^{1/(4\alpha-2)}\exp\left(-\frac{r^2}{(4\alpha-2)r_0^2}\right). \tag{3.8}$$

For the subsequent discussion, it is convenient to introduce the parameter $N=n_a/n_c$ denoting the ratio of the atomic gas density to the laser critical density. As has already been discussed in Sec. III A 1, the normalized vector potential can be put in the form

$$a_L^2=\frac{4\lambda^2}{\pi C}\left(\frac{P}{\pi r_0^2}\right)\exp\left(-\frac{r^2}{r_0^2}\right), \tag{3.9}$$

where $C=2mc^3/r_e=17.4$ GW. The constant C is the proportionality constant in the relation for the critical power $P_c=C\omega_L^2/\omega_p^2$, which from more accurate analysis of the relativistic self-focusing process [11] has been found to be $C=16.2$ GW. This last value has been used throughout the subsequent calculations. Introduction of Eq. (3.8) and Eq. (3.9) in Eq. (3.2) yields the total variation of the refractive index as

$$\eta(r,z)=1-\frac{q_0N}{2}\left(\frac{P}{\pi r_0^2}\right)^{1/(4\alpha-2)}\exp\left(-\frac{r^2}{(4\alpha-2)r_0^2}\right)\times\left[1-\frac{\lambda^2}{\pi C}\left(\frac{P}{\pi r_0^2}\right)\exp\left(-\frac{r^2}{r_0^2}\right)\right]. \tag{3.10}$$

Straightforwardly calculating the refractive index gradient from Eq. (3.10) and evaluating again for $r\approx r_0$ using the approximations $[\partial e^{-r^2/(4\alpha-2)r_0^2}/\partial r]_{r\approx r0}\approx -\{2r/[(4\alpha-2)r_0^2]\}\exp[-1/(4\alpha-2)]$, $[\partial e^{-r^2(4\alpha-1)/(4\alpha-2)r_0^2}/\partial r]_{r\approx r0}\approx -\{2r(4\alpha-1)/[(4\alpha-2)r_0^2]\}\exp[-(4\alpha-1)/(4\alpha-2)]$ and $\eta_0\approx 1$ the ray equation (3.3) becomes

$$\frac{d^2r}{dz^2}=\underbrace{+q_0N\frac{1}{4\alpha-2}\left(\frac{P}{\pi}\right)^{\frac{1}{4\alpha-2}}\frac{\kappa_0 r}{r_0^{\frac{4\alpha-1}{2\alpha-1}}}}_{refraction}\;\underbrace{-\frac{\lambda^2}{\pi C}q_0N\frac{4\alpha-1}{4\alpha-2}\left(\frac{P}{\pi}\right)^{\frac{4\alpha-1}{4\alpha-2}}\frac{\kappa_1 r}{r_0^{\frac{8\alpha-3}{2\alpha-1}}}}_{relativistic\ self\ focusing}\;+\underbrace{\frac{\lambda^2}{4\pi^2}\frac{r}{r_0^4}}_{diffraction}, \tag{3.11}$$

with $\kappa_0=\exp[-1/(4\alpha-2)]$ and $\kappa_1=\exp[-(4\alpha-1)/(4\alpha-2)]$ the corresponding position factors. Equation (3.11) gives the path of a ray $r(z)$ in the incoming pulse interacting with a gas. The three processes occurring during the interaction, namely (a) refraction, (b) relativistic self-focusing, and (c) diffraction are described by the corresponding terms clearly indicated in Eq. (3.11). As can be seen, the defocusing effect of the refraction and diffraction is counteracted by the relativistic self-focusing process. The relative contribution of each process for a specific gas is discussed in Sec. III B. It should be pointed out here that this model is valid strictly speaking for a Gaussian beam and for the case that transient ionization effects do not play any role [19,20]. For $r=r_0$ one obtains the ray tracing equation in a ionizing gas for the $1/e$ intensity radius of the beam. In this case, a first integral of the resulting equation can be easily obtained as

$$\left(\frac{dr_0}{dz}\right)^2 = \underbrace{-q_0 N\left(\frac{P}{\pi}\right)^{1/(4\alpha-2)}\frac{\kappa_0}{r_0^{1/(2\alpha-1)}}}_{refraction} \underbrace{+\frac{\lambda^2}{\pi C}q_0 N\left(\frac{P}{\pi}\right)^{(4\alpha-1)/(4\alpha-2)}\frac{\kappa_1}{r_0^{(4\alpha-1)/(2\alpha-1)}}}_{relativistic\ self\ focusing} \underbrace{-\frac{\lambda^2}{4\pi^2}\frac{1}{r_0^2}}_{diffraction} + \tan^2\theta_0. \tag{3.12}$$

The integration constant $\tan^2\theta_0$ is related to the incoming beam divergence defined as the cone with half-angle θ_0 (see also Sec. III B). Applications of Eq. (3.12) and comparison of its predictions with the experimental results are given in Sec. IV D.

3. Estimate of the charge distribution due to gas ionization

In the near field of the beam, there will be a threshold intensity above which the gas will start ionizing. This defines a region around the focal point inside which the gas is singly or multiply ionized. The prevailing intensity at each point would determine the ionization degree with the higher charge states located in regions of high intensity. This gives rise to ionization contours with the accompanying change in the index of refraction across these contours. To determine the charge state in a given gas as a function of intensity we follow the procedure described in Ref. [21].

In the tunneling regime characterized by values of the Keldysh parameter $\gamma<1$ [16] the intensity (in W cm^{-2}) required for an ion to be stripped of q electrons is given as [18]

$$I_q = 4\times 10^9\frac{U_q^4}{q^2}. \tag{3.13}$$

The ionization potential (in eV) of the ion with charge $q-1$ is denoted as U_q. To derive the expression in Eq. (3.7) for the calculation of the electron density profile, the assumption is made that the quantities I_q and U_q can be expressed in terms of continuous functions of q, i.e., $U(q)$ and $I(q)$. Furthermore, it is assumed that $U(q)$ can be given in the form of a power law:

$$U(q) = \hat{U}q^{\alpha}. \tag{3.14}$$

Introducing the relation in Eq. (3.14) into Eq. (3.13) and solving for q one obtains Eq. (3.7) with $q_0 = (4\times 10^9\hat{U}^4)^{1/(2-4\alpha)}$.

For the gases used in the experimental investigations, the values for the parameters $\hat{U}$ and α are obtained by least-square fitting the expression in Eq. (3.14) to the published data [43,44] for the ionization potentials of the different ionic species. The representation of the ionization potential as a smooth function of the ionic charge q is shown by the dashed lines in Fig. 2. The corresponding values of the parameters $(\hat{U},\alpha)$ for each gas are also given in the legend of the same figure.

Use of Eq. (3.7) with the appropriate parameters yields the ionic charge as a function of intensity. This is depicted in Fig. 3 where the ionic charge increases continuously with the intensity up to the point where the ionization saturates as in

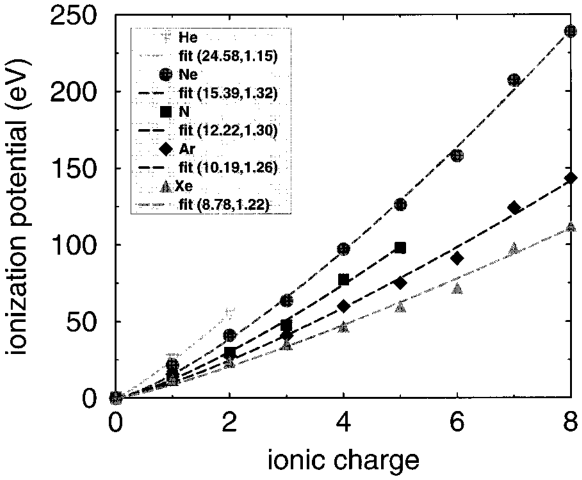

FIG. 2. Ionization potential for an ion with charge $q-1$. The points represent the published data for the ionization potentials of the indicated gases. The dashed lines are power-law fits of the form in Eq. (3.14) with the parameters $\hat{U}$ and α given for each gas in the inset.

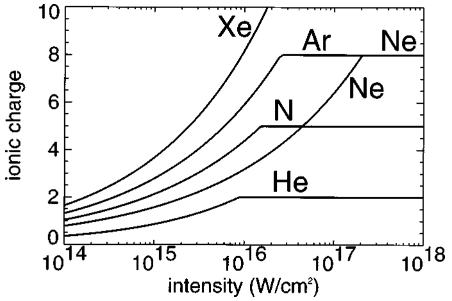

FIG. 3. Ionic charge q for the intensity range pertinent to the experiment.

the case of He or the energy gap to the next ionization stage is so large that intensities higher than 10^{18} W/cm^2 are needed to reach it. This occurs when a new shell (K shell for N and Ne and L shell for Ar) is reached.

The case of hydrogen is treated differently. From Eq. (3.13) it is easily seen that H becomes fully ionized at intensities above 1.4×10^{14} W/cm^2. Furthermore, it exhibits an extremely steep rise of the ionization rate as a function of intensity [17]. It is, therefore, reasonable to assume that for the experimentally attained intensities of $(3-5)\times10^{17}$ W/cm^2 the hydrogen gas is completely ionized and only at the very far wings of the beam is there still atomic hydrogen.

To obtain the path of a ray in an ionizing plasma, one has to distinguish between two regimes. For high intensities that lead to plateau ionization either because of saturation or because of the ionization potential gap between shells, Eq. (3.6) is used. For lower intensities where gradual ionization is occurring Eq. (3.11) is the appropriate one to describe the process.

B. Whole beam self-focusing in the presence of refraction

The interplay between relativistic self-focusing on one side and refraction and diffraction on the other side can be now quantitatively analyzed with the help of the ray tracing model developed in Sec. III A. For that purpose, Eq. (3.12) is the best starting point to gain insight into the different counteracting processes. According to the formulation of Ref. [41], the variation of the beam radius r_0 with distance can be perceived as the motion of a particle in a potential $V(r_0)$ for which a relation analogous to the energy conservation relation in the form

$$\left(\frac{dr_0}{dz}\right)^2+V(r_0)=\tan^2\theta_0 \tag{3.15}$$

is valid. Comparison of the above relation with Eq. (3.12) shows that the potential can be explicitly written as

$$\begin{aligned} V(r_0)= &+\underbrace{q_0N\left(\frac{P}{\pi}\right)^{1/(4\alpha-2)}\frac{\kappa_0}{r_0^{1/(2\alpha-1)}}}_{refraction}\\ &-\underbrace{\frac{\lambda^2}{\pi C}q_0N\left(\frac{P}{\pi}\right)^{(4\alpha-1)/(4\alpha-2)}\frac{\kappa_1}{r_0^{(4\alpha-1)/(2\alpha-1)}}}_{relativistic\ self\ focusing}\\ &+\underbrace{\frac{\lambda^2}{4\pi^2}\frac{1}{r_0^2}}_{diffraction}\ . \end{aligned} \tag{3.16}$$

It should be pointed out here that our definition of the potential $V(r_0)$ differs from that used in Ref. [41] by a factor of $2\pi/\lambda$. Again, the contributions of each of the three processes involved are shown explicitly in Eq. (3.16) and are plotted for two cases (low and high density) along with the potential $V(r_0)$ in Fig. 4.

The interpretation of the plot in Fig. 4 is as follows: far away from the focal point located at $z=0$ the potential $V(r_0)$ approaches zero, and from Eq. (3.15) it is easily seen that $dr_0/dz\approx\pm\tan\theta_0$, i.e., the initial beam convergence or divergence. As z moves towards the focal point, the beam radius is reduced, which has as a consequence the increase of the potential and the decrease of the local beam convergence. This will continue until $dr_0/dz=0$, i.e., until the beam has reached the minimum possible radius. Subsequently, the beam will start to expand again. This is in analogy to a particle moving in the potential shown by the solid line in Fig. 4. For a given initial velocity it will move uphill in the direction of smaller radii reaching a maximum height and then it will roll down again in the direction of larger radii. It is obvious that if the particle has an initial velocity slightly greater than a critical one corresponding to the maximum of the potential hill, it would be able to overcome the barrier and fall into the hole around $r_0\sim0$. For the beam development that means that if the initial beam convergence has a value greater than the maximum of the potential $V_{\max}$ in Fig. 4, it will collapse to zero radius. In a more realistic model which includes saturation of the self-focusing mechanism [11], the potential curve would exhibit a minimum with the consequence that the beam radius depending on the initial conditions would oscillate between a minimum and a maximum value [41].

Therefore, for a given wavelength λ, beam power P, density N, and gas parameters q_0,α one obtains the minimum achievable $1/e$ intensity radius of the beam $r_{0,\min}$ by setting $dr_0/dz=0$ in Eq. (3.15) and solving the algebraic equation $V(r_{0,\min})=\tan^2\theta_0$. For an initial beam diameter $D=2w_{0,\mathrm{init}}=2\sqrt{2}r_{0,\mathrm{init}}$ and focusing optics with focal length f the corresponding F number customarily defined in terms of the beam waist [45] is given as $F_{\#}=D/f=2\sqrt{2}r_{0,\mathrm{init}}/f$. Thus, the initial beam convergence is connected to the $F_{\#}$ of the focusing optics through the relation $\tan\theta_0=(2\sqrt{2}F_{\#})^{-1}$. Furthermore, if the initial beam convergence dr_0/dz is greater than the maximum value of the potential $V_{\max}=V(r_{0,c})$ the beam will self-focus to zero radius.

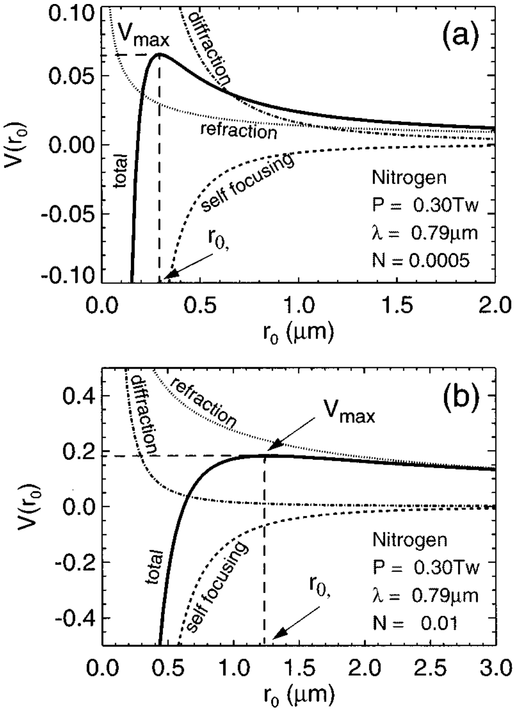

FIG. 4. Plot of the potential in Eq. (3.16) as a function of the beam radius r_0 for nitrogen. (a) For low density, (b) for high density.

From the specific example depicted in Fig. 4, one sees that, for large radii, refraction is dominant. As the beam radius shrinks the self-focusing mechanism becomes important and, for low densities [Fig. 4(a)] it is the competition between diffraction and self-focusing that determines the minimum radius while, for high densities [Fig. 4(b)] refraction and self-focusing are the dominant processes. It should be pointed out here that although the parameters used to calculate the potential curves in Fig. 4 are pertinent to the experimental data, nevertheless the situation represented does not correspond to the experimental situation since it assumes that the ionizing gas is present along the whole path of the beam while in the experiment a puff valve was used.

1. *Condition for self-focusing and the effect of the ionization plateau*

It is interesting now to explore under what conditions one can expect to observe self-focusing despite the presence of the refraction. In the previous section such a condition was already found albeit in an implicit form. It was concluded that when $(dr_0/dz)^2=\tan^2\theta_0>V_{\max}=V(r_{0,c})$ then the beam will self-focus. A more useful condition in terms of the density N can be obtained if the value of $V_{\max}$ is explicitly calculated. This can be performed only approximately for the high density case where refraction dominates if the last term in Eq. (3.16) representing the process of diffraction is omitted. As can be seen from Fig. 4(b), this is reasonable since we are primarily interested in the region where refraction dominates. Taking the derivative of the potential function and solving the equation $dV(r_0)/dr_0=0$ one obtains the critical radius $r_{0,c}$ for which the potential exhibits its maximum. Substitution of $r_{0,c}$ back into the potential function yields the maximum value as

$$V_{\max}=q_0N\frac{4\alpha-2}{4\alpha-1}\left(\frac{\pi C}{\lambda^2(4\alpha-1)}\right)^{1/(4\alpha-2)}. \tag{3.17}$$

The requirement for self-focusing that the initial beam convergence is larger than this maximum value of the potential gives an upper limit for the gas density in the refraction dominated case, i.e.,

$$N<N_B=\frac{\tan^2\theta_0}{q_0[(4\alpha-2)/(4\alpha-1)][\pi C/\lambda^2(4\alpha-1)]^{1/(4\alpha-2)}}. \tag{3.18}$$

It might appear surprising that the expression for $V_{\max}$ in Eq. (3.17) and consequently, the critical density for self-focusing in Eq. (3.18) are independent of the beam power P. In part this is due to the fact that both, the refraction and the self-focusing term in the original expression for the index of refraction in Eq. (3.2) are proportional to N. While $r_{0,c}$ where the potential has its maximum value is a function of the power P, once the value of $V_{\max}$ is evaluated the peak value is independent of P. The meaning of the condition in Eq. (3.18) is that for gas densities higher than N_B self-focusing cannot occur under any circumstances. For gas densities lower than this critical value, self-focusing will occur if in addition the condition $P>P_c$ is satisfied, which in turn sets a lower density limit N_A dependent on the laser power P_L. It is easily deduced that this limit would be $N_A=C/(\kappa q_{\max}P_L)$.

From this analysis, it follows that for a given laser power P_L and a specific gas target there exists a gas density range $N_A<N<N_B$ for which an ideal Gaussian beam will exhibit self-focusing. Outside this density *window* no self-focusing can occur and more specifically, for $N<N_A$ diffractive defocusing while for $N>N_B$ refractive defocusing would dominate over the self-focusing mechanism.

In the previous discussion, the effect of the ionization plateau exhibited by different gases (see Fig. 3) has not been taken into account. The saturation of the ionic charge to its maximum value $q_{\max}$ due to either full ionization or ionization potential jumps between atomic shells may result in a saturation value for the potential function before the maximum value given by Eq. (3.17) can be reached. This means that the condition for self-focusing becomes more favorable since higher intensities do not produce index of refraction gradients. An estimate of the saturated value for the potential can be easily found with the help of Eq. (3.7) from which the relation $I=P/(\pi r_0^2)=(q_{\max}/q_0)^{4\alpha-2}$ is obtained. Introduction of this value for the power into the refraction term in the Eq. (3.16) renders the saturated value of the potential, which in turn gives a new condition for self-focusing in the form

$$N<N_B^{\mathrm{sat}}=\frac{\tan^2\theta_0}{q_{\max}\kappa_0}. \tag{3.19}$$

This last relation is in accordance with the electron density estimate at which refraction-induced density clamping becomes important. It was found in earlier work [19,22] that for a Gaussian beam this electron density is approximately given by $n_e=n_c\tan^2\theta$, which apart from the position factor κ_0 is identical to the one in Eq. (3.19). For small incident

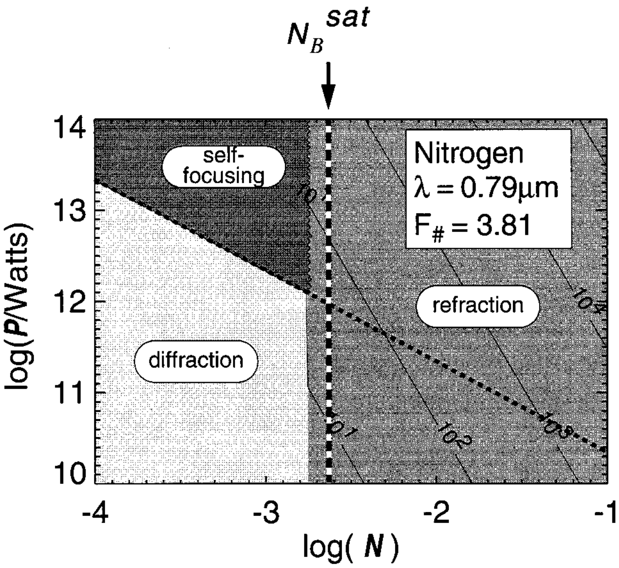

FIG. 5. The P-N diagram for the case of a Gaussian beam with the indicated parameters propagating in nitrogen. Depending on the power P of the beam and the density of the gas N, the final minimum radius would be determined by the dominant process, i.e., diffraction or refraction or self-focusing. The contours indicate the minimum achievable radius in μm in the refraction dominated regime. The vertical dashed line indicates the upper limit for the gas density as predicted by Eq. (3.19). The diagonal dashed line represents the transition to self-focusing according to the relation $P=C/(\kappa q_{\max} N)$.

angles, a similar relation is obtained from Snell's law if one calculates the maximum electron density to which a ray incident into an electron density gradient profile at an angle θ can penetrate due to refraction, i.e., $n_e \approx n_c \theta^2$. In essence propagation cannot proceed to higher electron densities because refraction will turn the ray outwards at this maximum density value. To verify these predictions and to map out in the P-N diagram the different regions characterized by a specific process, we have solved numerically the algebraic equation $V(r_0)=\tan^2\theta_0$ to determine the minimum $1/e$ intensity radius $r_{0,\min}$. This time the full expression for $V(r_0)$ as given by Eq. (3.16) was employed. To include the effect of the ionization saturation, the corresponding potential function for the case of fully ionized plasma obtained from Eq. (3.6) was used whenever the ionic charge would rise to values $q > q_{\max}$.

A specific example of such a P-N diagram for nitrogen (the gas that was mostly used in the experiments) is shown in Fig. 5. It is seen that the exact solution predicts a transition from the refraction regime to diffraction and self-focusing regime very close to the density value calculated by Eq. (3.19). For densities $N > N_B^{\mathrm{sat}} \approx 2.0 \times 10^{-3}$, the beam propagates in an environment where multiply ionized nitrogen up to N^{5+} exists, giving rise to a strong refraction index gradient. As a consequence, the minimum beam radius does not reach the diffraction limited value and no self-focusing can occurs. For lower density values than N_B^{sat}, the well-known self-focusing condition $P > P_c/\kappa$ must be satisfied in order to observed self-focusing. For the specific example in Fig. 5, the nonsaturated value for N_B as calculated by the expression in Eq. (3.18) is 5×10^{-4}. It is therefore, important to consider the effect of the ionization saturation as it can considerably increase the self-focusing density window.

The usefulness of the criterion in Eq. (3.18) or Eq. (3.19) is obvious since for a given gas it allows the estimation of the density window for achieving self-focusing when a certain laser power is available. Evidently, hydrogen would be in any case the best choice of gas to observe self-focusing at high gas densities and low laser power. However, the diagram in Fig. 3 in connection with Eq. (3.19) suggests immediately that helium would be the next most favorable gas followed by nitrogen and so on.

C. Beam interaction and propagation in a gas jet

As has been already pointed out, all the previous discussion deals exclusively with the case of a static-filled interaction chamber. Although this is useful in order to separate and study the different processes, these results cannot be directly compared with the experimental measurements that were made mostly using a gas jet. The gas jet limits the spatial extent of the beam interaction with the gas to a small volume around its nozzle. Therefore, the beam propagates undisturbed from the focusing optic to the interaction region where it starts interacting with a spatially varying gas density volume.

In this section we present a more realistic modeling of the experimental situation, which also delivers quantitative results directly relevant to the measurements. However, this requires the solution of the paraxial ray equation in Eq. (3.11) or, whenever the ionic charge exceeds the saturation value of the corresponding gas (see Fig. 3), in Eq. (3.6). For the particular jet used in these experiments [33] it has been found that the gas density at a distance of ~ 300 μm from its orifice can be adequately modeled by a simple Gaussian profile of the form $N(z)=N_0 e^{-2.77[(z-z_{\mathrm{jet}})/d_{\mathrm{jet}}]^2}$. Here z_{jet} is the position of the vacuum focus location with respect to the jet axis, d_{jet} is the extent [full width at half maximum (FWHM)] of the gas plume in the beam propagation direction and N_0 is the peak gas density, which is proportional to the backing pressure (see also Sec. II). This spatial dependence of the gas density is introduced in Eq. (3.11) and Eq. (3.6), which is then solved using numerical procedures. The solution gives the spatial variation for $r=r_0$, i.e., for the $1/e$ intensity radius of the beam. As initial conditions the beam radius and convergence at a large distance from the jet location ($z_i=5d_{\rm jet}$) are used assuming a Gaussian beam propagating in vacuum and having a confocal parameter $w_0=2\lambda F_\#/\pi$.

For experimentally relevant parameters ($F_\#=3.8$, $\lambda=0.79$ μm, $P=0.3$ TW, $d_{\rm jet}=525$ μm, and $z_{\rm jet}=115$ μm) the beam behavior for four different peak nitrogen densities is depicted in Fig. 6. It is seen that for low peak gas densities [Fig. 6(a)] the beam penetrates the gas jet to a point beyond the vacuum focus. At slightly higher densities [Fig. 6(b)], the self-focusing mechanism manifests itself clamping the beam radius down to a value that depends on the saturation mechanism present (not included in the model). Higher densities [Figs. 6(c) and 6(d)] force the interaction into the refraction regime. The exhibited shallow penetration of the beam and its strong deflection is a consequence of the ionization-induced defocusing.

To relate the prediction of the model with the experimental results, we have plotted in Fig. 7 four quantities that show the overall behavior of the interaction with increasing gas density. From Fig. 7(a) it is seen that the minimum achievable beam radius decreases at the beginning with density until the interaction reaches the self-focusing regime after which it increases monotonically. The position of the focus [Fig. 7(b)] moves away from the focusing optics at the beginning but then moves towards it and finally saturates at a particular value. The beam size at 250 μm past vacuum focus, d_{250} (FWHM) [Fig. 7(c)] shows a similar dependence on the minimum beam radius but a more dramatic increase with density. The Rayleigh range that relates to the observable interaction region length between the 50% intensity points on axis and it has been used as experimental evidence for self-focusing exhibits a similar increase with the density. A more quantitative comparison of the model predictions with the experimental data is given in Sec. IV D.

IV. EXPERIMENTAL RESULTS

A. Characterization of the focal beam profile

The interplay between the focusing and defocusing mechanisms strongly depends on the actual beam profile near the focal region of the beam. Therefore, an interpretation of the experimental results requires the detailed knowledge of the radial beam intensity distribution at the entrance of the interaction region around the gas jet.

The radial beam profile is determined primarily by the quality of the focusing optical element. The diamond turned 90° off axis parabola used in these experiments had a nearly perfect parabolic shape, but the cutting process had left tool marks with a peak-to-valley amplitude ratio of the order of ~0.33 μm. This structure acted as a grating dispersing a considerable amount energy into the first order left and right of the focal point and in the perpendicular direction to the reefs. A considerable improvement was achieved by hand polishing the parabolic surface. However, this led to some degradation in the parabolic shape. In the final form the parabolic mirror was tested using a single mode HeNe laser and the equivalent focal plane technique to measure the spot size.

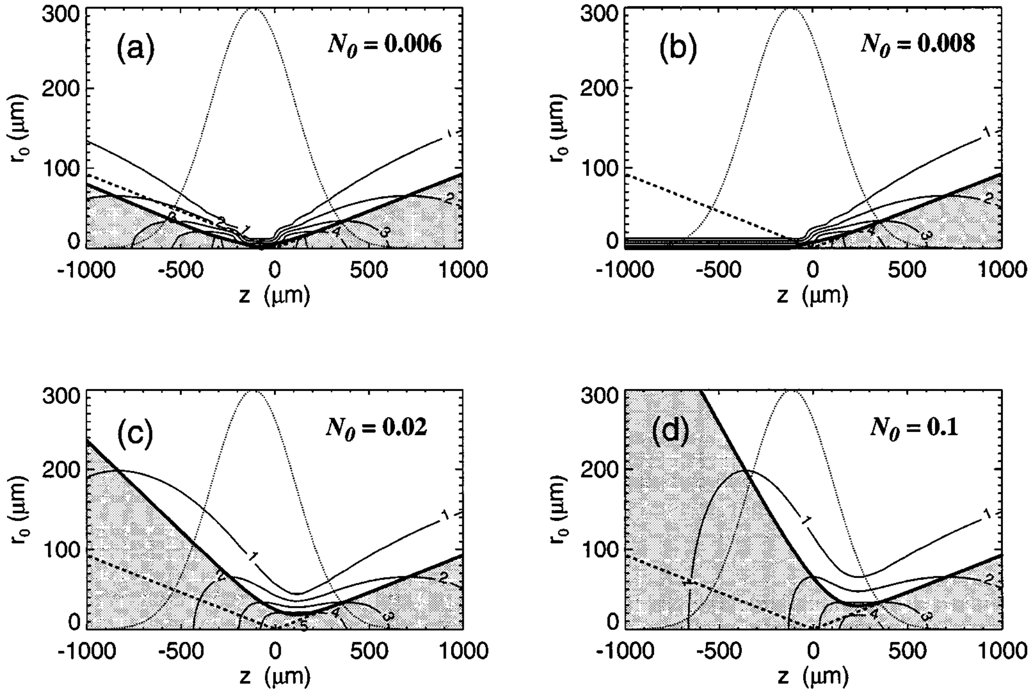

FIG. 6. Variation of the beam radius r_0 with the distance from the vacuum focus ($z=0$) of a beam interacting with a finite extent nitrogen jet. The solid line gives the variation of the $1/e$ intensity radius of the beam in the presence of the gas jet, the dashed line is the corresponding variation in vacuum with the beam entering from the right hand side, the dotted line represents the density variation $N(z)/N_0$, and the thinner solid lines are the ionization contours. (a) Low density regime, (b) self-focusing regime (for numerical reasons the radius after self-focusing has been clamped to 1/10 of the diffraction limited radius), (c) refraction dominated regime, and (d) the beam is strongly refracted.

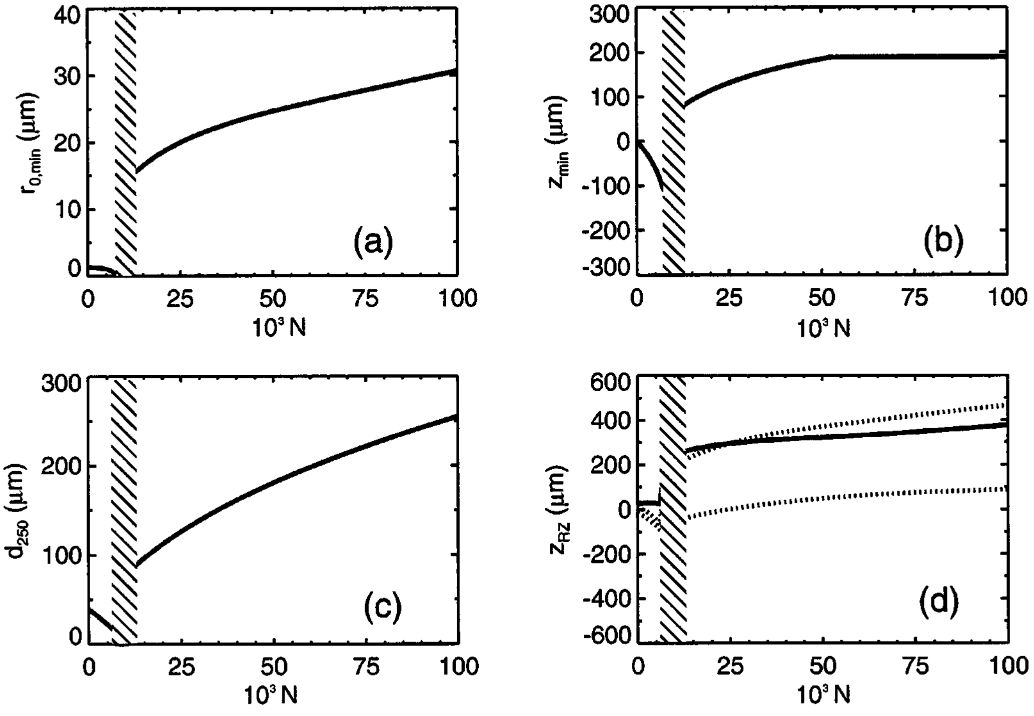

FIG. 7. Variation with density of the (a) minimum radius, (b) its location, (c) beam diameter $d_{250}=1.66r_{0,250}$, and (d) Rayleigh zone for nitrogen gas jet. The dotted lines in (d) give the location of the beam where its radius is $\sqrt{2}r_{0,\min}$. The shaded area indicates the self-focusing region. The same input parameters as in Fig. 6 were used for the calculations.

A high resolution multiple element objective with $F_{\#}=2.5$ and $f=10$ cm was employed to image the focal spot plane into a CCD camera with a magnification factor of ~ 23 and a spatial resolution of ~ 1 μm. The overall dynamic range of the CCD camera was extended using several neutral density (ND) filters and numerically combining records taken under different exposure conditions. The result of these measurements is shown in Fig. 8(a). As can be seen, there is a peak of high intensity surrounded by a broader, lower intensity region, which primarily extends in one direction. In order to specify the focal spot profile more accurately, we have employed the record shown in Fig. 8(a) to numerically perform the integration $P_{\exp}(r)=\int_0^r\int_0^{2\pi}I_{\exp}(\rho)\rho d\rho d\phi$ and obtain the azimuthally averaged power within a radius r. The result is given in Fig. 8(b) by the points. One immediate observation is that the half beam energy is confined in a spot size having a radius of ≈ 10 μm. What is of interest here is the actual intensity distribution. This is approximately obtained by fitting a double Gaussian profile of the form $P_f(r)=c(1-e^{-(r/r_{f,a})^2})+(1-c)(1-e^{-(r/r_{f,b})^2})$ to the experimental data for the power. This corresponds to a double Gaussian intensity profile of the form: $I_f(r)=I_{f,a}+I_{f,b}=ce^{-(r/r_{f,a})^2})+(1-c)e^{-(r/r_{f,b})^2}$. Here, the relative amplitude of the two Gaussian profiles c and their $1/e$ intensity radii are the free parameters used for the fitting. The thus obtained power P_f and intensity distribution I_f are shown in

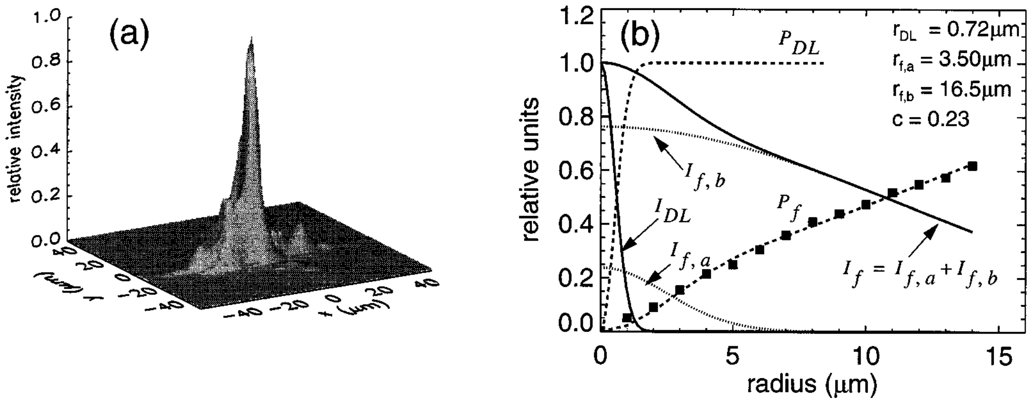

FIG. 8. Focal spot characterization. (a) Measured focal spot profile using a single mode HeNe laser and the equivalent focal plane technique. (b) The points represent the power contained within a circle of radius r and it is obtained from the integration over the angle of the record in (a). The dashed line through the point is a least-square fit of a double Gaussian profile (see discussion in the text). The corresponding intensity profile I_f is the solid line and it consists of two Gaussians (dotted lines). The solid line marked I_{DL} gives for comparison the diffraction limited intensity profile for the case of $\lambda=0.63$ μm and $F_{\#}=2.55$.

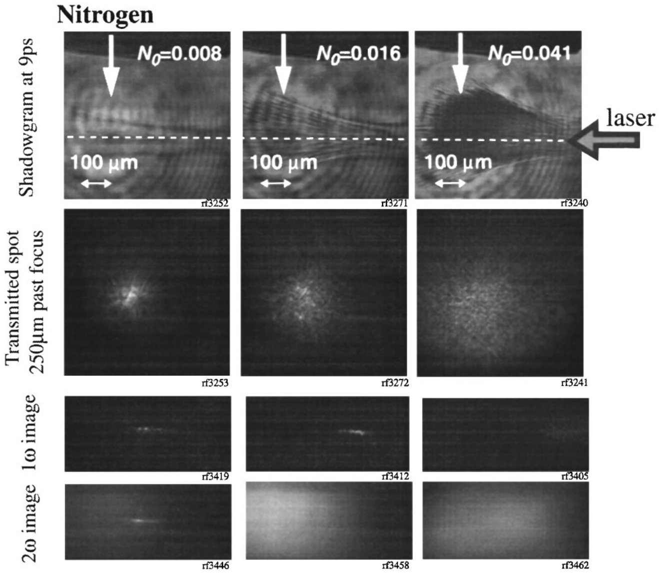

FIG. 9. Images of the interaction of the 0.3 TW laser pulse with a 500 μm diameter nitrogen gas jet at various peak atomic densities. The top row of pictures are shadowgrams taken with a 2ω probe pulse. The second row shows images of the transmitted light spot at a position 250 μm past the focal position. The third and fourth rows show images taken of the 1ω and 2ω emission viewed perpendicular to the axis of the main laser beam. In the side-on images, the laser is incident from the right and the gas jet is at the top with its center at a position approximately indicated by the white arrow. The length scale for all images is given in the inset in the top images.

Fig. 8(b). For comparison, the diffraction limited intensity profile corresponding to the nominal value of $F_{\#}=2.55$ for the parabolic mirror and the HeNe laser wavelength is shown in the same figure. As can be seen, the actual beam profile at focus deviates considerably from the diffraction limited value. The fitting procedure quantitatively confirms the experimental observation, i.e., that the focal spot profile consists of a broad background intensity with a $1/e$ intensity radius of 16.5 μm on the top of which there exists a peak with 3.5 μm radius. These values are expected to be somewhat higher for the Ti:sapphire laser beam because of the slightly longer wavelength and the poorer beam quality. However, the measured Ti:sapphire beam characteristics of a 5 μm (FWHM) diameter central spot and a 50% energy containing diameter of 20 μm agree well with the above profile. As discussed in Sec. IV D the influence of the focal spot profile on the beam interaction processes with the gas jet is decisive for the occurrence of self-focusing in the case that refractive defocusing plays a role.

B. Shadowgraphy and time-integrated images

Four sets of images were measured experimentally for each gas at various atomic densities ranging from $0.01n_c$ to $0.20n_c$. These included the shadowgram taken with the second harmonic probe pulse, the fundamental radiation transmitted through the gas jet imaged at a point 250 μm past the vacuum focal position, and the self-emission images taken from right angles to the direction of propagation at both the fundamental and second harmonic wavelengths. The shadowgrams and transmitted images were taken simultaneously on the same laser shots while the self-emission images were recorded on separate laser shots with the probe beam blocked and suitable interference filters in place.

The shadowgrams were taken with the imaging system focused on the axis of the laser beam in vacuum to within an accuracy of ± 25 μm. Features in the image that contain large electron density gradients and thus large refractive index gradients such as the edge of the ionized plasma region or filamentary density structures refract part of the probe light outside the $F_{\#}=2.5$ collection cone angle of the imaging system. These then cause shadow regions in the image. Also refracting features that are located significantly in front of or behind the focal plane produce dark and bright regions in the image since the refraction they cause is not corrected by the imaging system. In the shadowgraphic images modulations in the background illumination are visible due to imperfections in the probe laser wave front. These are caused by the nonuniform near field profile of the femtosecond laser pulse enhanced by the frequency doubling process and diffraction rings from aperturing of the probe beam by optical elements. These features are visible in the probe beam when shots are taken in vacuum with no gas jet present and thus can easily be distinguished from the density structures from the plasma.

A sequence of images for nitrogen gas at three different gas densities is shown in Fig. 9. For the side-on images the laser enters from the right and the gas jet nozzle is located above. The laser passes by the nozzle at a distance of ~300 μm from the nozzle exit. In the shadowgram images the edge of the nozzle is visible at the top of the image and the vacuum axis of the laser is shown as a dashed line. The position of the peak density of the gas jet is indicated by an arrow and the vacuum focus is located to the right of the peak density position by 115 μm. The shadowgrams were taken at 9 ps after the leading edge of the pulse has reached the vacuum focus position. Thus, the images give a snap shot of the ionized plasma produced by the interaction after the interaction has finished but before any significant expansion of the plasma can occur. For $N_0=0.008$ only a faint outline of the breakdown plasma is observed. Because of the low density the density gradients are moderate and the refractive effects of the density features are small. The observed outline of the plasma is approximately symmetrical around the laser axis. At a higher density of $N_0=0.016$ the outline of the ionized plasma region is clearly visible and filamentary structures can be seen inside the ionized plasma. It is expected that the edges of the shadowgraphic image correspond to the singly ionized outer edges of the plasma region. Asymmetry in the plasma structure is observed with more deflection and curvature towards the gas nozzle than away from the gas nozzle. This arises from the gradient in the background gas density, which decrease in the direction away from the nozzle. Thus the upper part of the beam propagates through significantly higher gas density than the lower part of the beam. At a much higher density of $N_0=0.041$ the transverse size of the plasma has increased again and the asymmetry is even more pronounced than in the previous images. Whereas at lower pressures it appears that the ionized plasma continues to the edge of the field of view, in the highest density case the absorption and refraction is so strong that the main part of the plasma terminates

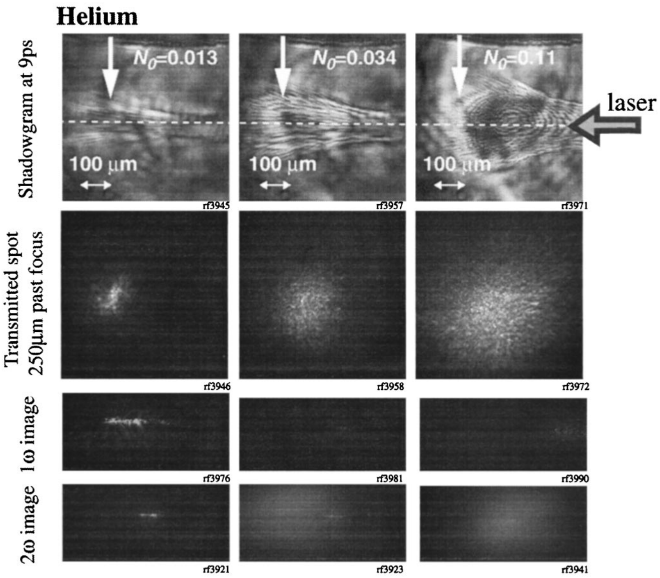

FIG. 10. Images of the interaction of the 0.3 TW laser pulse with a 500 μm diameter helium gas jet at various peak atomic densities. The top row of pictures are shadowgrams taken with a 2ω probe pulse. The second row shows images of the transmitted light spot at a position 250 μm past the focal position. The third and fourth rows show images taken of the 1ω and 2ω emission viewed perpendicular to the axis of the main laser beam. In the side on images, the laser is incident from the right and the gas jet is at the top with its center at a position approximately indicated by the white arrow. The length scale for all images is given in the inset in the top images.

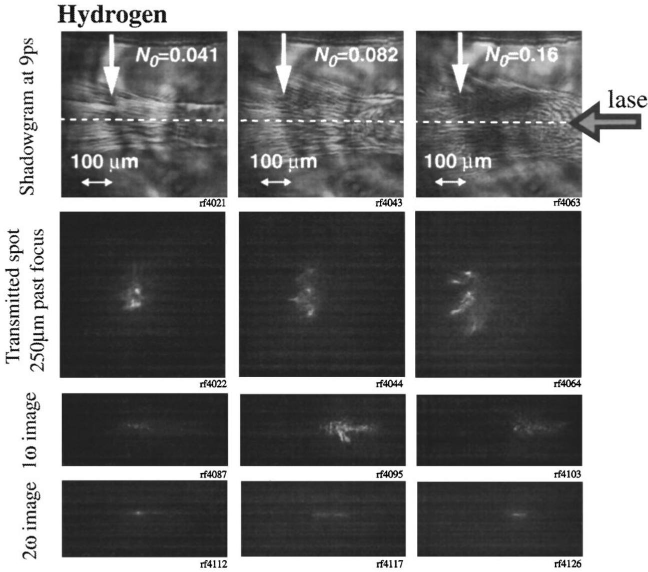

FIG. 11. Images of the interaction of the 0.3 TW laser pulse with a 500 μm diameter hydrogen gas jet at various peak atomic densities. The top row of pictures are shadowgrams taken with a 2ω probe pulse. The second row shows images of the transmitted light spot at a position 250 μm past the focal position. The third and fourth rows show images taken of the 1ω and 2ω emission viewed perpendicular to the axis of the main laser beam. In the side-on images, the laser is incident from the right and the gas jet is at the top with its center at a position approximately indicated by the white arrow. The length scale for all images is given in the inset in the top images.

at about 100 μm before the edge of the field of view. One can still observe a few filaments of light propagating beyond the edges of the main plasma region. The shape of the terminating edge of the main plasma is also asymmetric occurring earlier nearer the gas jet nozzle than the side farther from the gas jet nozzle. This would agree with enhanced refraction from the higher density region of the gas jet spreading the beam more and causing the average flux to drop below the single ionization threshold of nitrogen. Also the dark region in the tail end of the plasma indicates significant absorption of the probe beam in the large, cold high density plasma.

The images taken of the transmitted laser spot 250 μm past focus show that at low densities the spot is of the same size as the vacuum spot but that at higher densities the diameter expands as the transmitted spot is more and more refracted. In addition, the overall distribution of the transmitted light becomes quite smooth with a filamentary substructure. The filamentary appearance is similar to the filamentary appearance seen in the shadowgrams.

The self-emission 1ω images give a different view of the interaction highlighting the high intensity central region of the laser pulse. The 1ω images show the expected shift in the peak field region towards the incoming laser beam at higher gas densities. Quantitative comparisons of the position of peak emission versus gas density will be presented later in Sec. IV D together with comparisons to model calculations. The transverse diameter of the emission region is approximately 15–20 μm at the lower density. The emission shows highly modulated intensity regions that vary randomly from shot to shot. These bright spots probably are indicative of weak stimulated Raman scattering enhancing the Thomson scattered light by one or more orders of magnitude. Also, one can observe faint filamentary structures coming out of the main emission region at a slight angle to normal. At the highest densities the bright regions disappear and the emission becomes more uniform and diffuse filling in the expected angular cone of the refracted incoming laser beam.

The 2ω emission images also highlight the most intense part of the laser-plasma interaction. However, the strength of the 2ω emission is much less than that of the fundamental scattered light and thus at higher densities the self-emission of the plasma becomes equal in brightness to the second harmonic signal. This time integrated background emission comes from the expanding blast wave in the gas and is normally emitted over a time of several nanoseconds. The brightness of this background emission is a function primarily of the deposited energy per unit length in the plasma weighted by the plasma density. One can see that for the lowest density image the emission is peaked near the peak of the gas jet density to the left of the position of the vacuum focus. The background emission shifts towards the incoming laser beam at the higher gas densities. The position of the 2ω signal cannot be observed at the higher densities above approximately $N_0=0.01$ because the increase in density results in higher plasma emission, which obscures the weak second harmonic emission signal.

A similar set of images is shown for helium gas in Fig. 10. In this case because the helium will be doubly ionized as compared to five times ionized for nitrogen gas the same

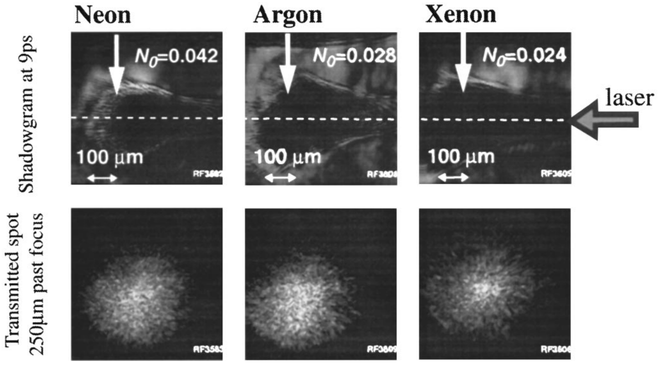

FIG. 12. Images of the interaction of the 0.3 TW laser pulse with various 500 μm diameter gas jet targets at various peak atomic densities. The top row of pictures are shadowgrams taken with a 2ω probe pulse. The second row shows images of the transmitted light spot at a position 250 μm past the focal position. In the side-on images, the laser is incident from the right and the gas jet is at the top with its center at a position approximately indicated by the white arrow. The length scale for all images is given in the inset in the top images.

degree of peak ionization and comparable refraction is expected for atomic densities approximately 2.5 times greater than those for nitrogen. The three cases shown correspond to approximately 1.6–2.7 times the atomic densities of the nitrogen gas cases shown in Fig. 9. In the same manner as for nitrogen the transverse size of the plasma increases at higher densities due to the increased refractive spreading of the beam. Similar filamentary structure is observed within the plasma region. Asymmetry in the refraction at higher intensities is less pronounced than for nitrogen and is only slightly apparent in the shadowgram for $N_0=0.11$. However, the truncation of the plasma breakdown in the middle of the gas jet occurs earlier than for nitrogen at the highest density shown. This is probably due to the much higher intensity required to singly ionize helium compared to nitrogen and thus as the beam refracts it drops below the necessary intensity to ionize the helium gas sooner than for nitrogen. Again a few individual filaments propagate beyond the end of the bulk plasma. The plasma for the high density case is also not as dark as that of nitrogen indicating less absorption of the probe beam in the lower atomic number plasma.

The images of transmitted radiation at 250 μm past the vacuum focal position look very similar to those for nitrogen showing a uniform diffuse image with increasing diameter from refraction at higher densities with filamentary substructure.

The 1ω images show bright structured emission on axis together with weaker filaments branching out sideways. Again a shift is seen in the center of the emission region first away from the laser at low pressures and then towards the laser at higher pressures. Randomly scattered bright spots are observed on each shot for the middle and low density shots again indicative of some stimulated Raman scattering enhancing the normal Thomson scattering.

The 2ω images show peak emission near the vacuum focal position at the lowest density and then a shift back towards the laser at higher densities. The background plasma emission is less from helium than nitrogen and thus the second harmonic signal is visible up to higher equivalent electron densities than for nitrogen. However, at the highest density shown the emission becomes strong enough and the second harmonic signal weak enough that it is no longer visible. For the highest density case the emission is seen to shift forward to the first half of the gas jet where the plasma is also observed in the shadowgram.

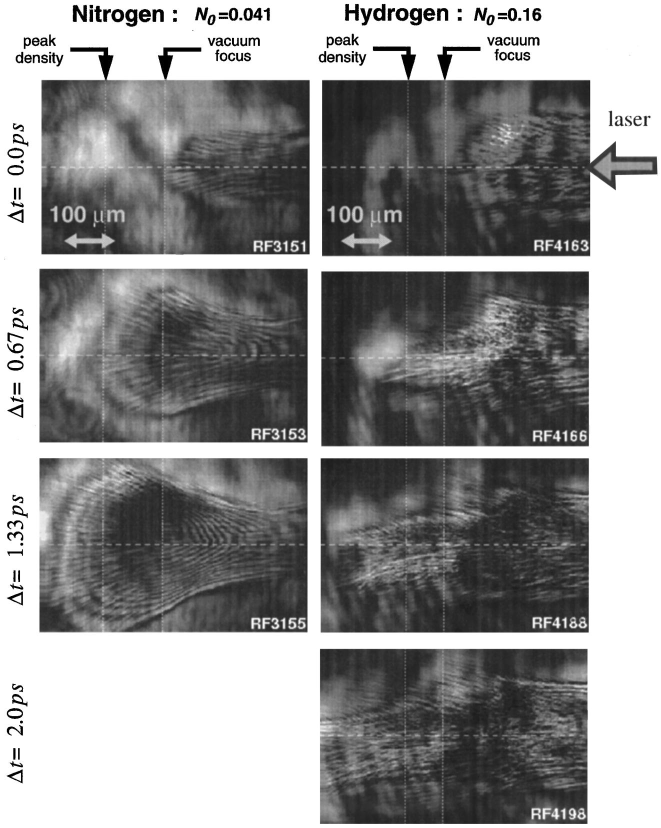

FIG. 13. Shadowgrams taken at various times throughout the interaction of the laser and the gas jet for nitrogen and hydrogen gas.

A set of images under similar conditions is shown in Fig. 11 for hydrogen gas at atomic densities of $N_0=0.041-0.16$. In this case the images show different behavior as compared to the other gases. The shadowgrams taken 9 ps after the laser interaction show increasing plasma diameter with density. However, the ionization region does not terminate prior to the end of the field of view showing propagation at ionizing intensities throughout the gas jet. This is expected since the ionization threshold is very low (1.5×10^{14} W cm^{-2}) and the absorption appears to be significantly less than for nitrogen, which has a similar ionization potential. The filamentary structure in the shadowgrams appears even more pronounced and chaotic than for the previous gases and, as will be shown later, there is considerably more structure visible at earlier times just at the end of the interaction period.

The most interesting observations for hydrogen gas come from the transmitted images at 250 μm past focus where several hot spots are observed in the transmitted radiation. This structure is completely different from that observed with all the other gases studied in this experiment and are indicative of large scale channeling of parts of the laser beam. The observed structures are similar from shot to shot,

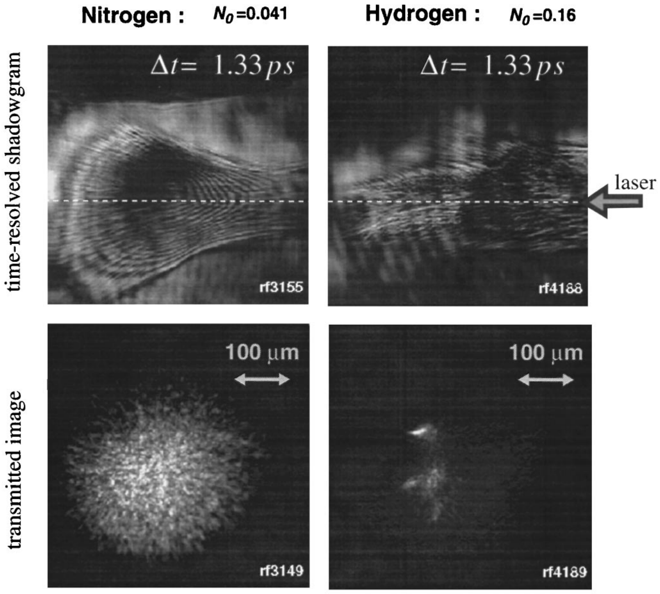

FIG. 14. Direct comparison of the shadowgram and transmitted spot images underlining the radically different behavior of the interaction for nitrogen and hydrogen.

indicating that the channeling is seeded by modulation in the laser beam profile itself.

The 1ω images are also characteristically different from the other gases. They show less of a shift with density and also become more spread out in size laterally than for the other gases. The images also show even more pronounced lateral structure than for the other gases. Again, randomly distributed bright hot spots are observed indicative of stimulated Raman enhancement of the Thomson scattered light.

The 2ω images are also characteristically different from other gases. A slight shift in the peak emission region towards the laser is observed with increasing density. However, the 2ω emission is stronger than the background plasma emission for all densities investigated. At the intermediate densities of the order of $N_0 = 0.08$ a fine line filament is observed in the emission image. The width of this line is on the order of 2–4 μm with a length of 65 μm, which is finer than the focal spot of the laser beam over this distance. Images of the second harmonic emission for other gases are somewhat broader with widths of $7-10$ μm and not as long as the image shown here. In summary, the second harmonic emission is indicative of a narrow filament region while the fundamental emission predominantly occurs outside of this narrow central region.

Other gases were also studied and their behavior in general is similar to that of nitrogen. Typical shadowgrams and transmitted radiation images at 250 μm past focus are shown in Fig. 12 for neon, argon, and xenon. All three of these gases will ionize to higher peak ionization states than nitrogen of 8^+ for neon for peak intensities of over 2×10^{17} W cm^{-2}, 8^+ for argon at 3×10^{16} W cm^{-2}, and over 12^+ for xenon at over 4×10^{16} W cm^{-2} (see Fig. 3). However, the first ionization energy of neon is above that of nitrogen while that of argon and xenon are below that of nitrogen. The shadowgrams are shown for the higher density cases of the three gases which qualitatively demonstrate the same features as nitrogen does at similar densities.

In particular all three gases show a termination of the plasma breakdown region within the field of view and still in the main part of the gas jet. The higher atomic number gases show darker images indicating more absorption of the probe beam in the cold ionized plasma. Neon terminates somewhat sooner than nitrogen for $N_0 = 0.042$, which agrees with the much higher first ionization energy than nitrogen. Argon terminates about at the same point as nitrogen even though its first ionization potential is less than nitrogen and the atomic density is only 60% of that of nitrogen. Xenon shows ionization farther through the gas jet as would be expected since it has the lowest first ionization potential of all the gases studied. All the gases show a filamentary structure both in the shadowgrams and the images of transmitted radiation at a position of 250 μm past focus. These images of transmitted

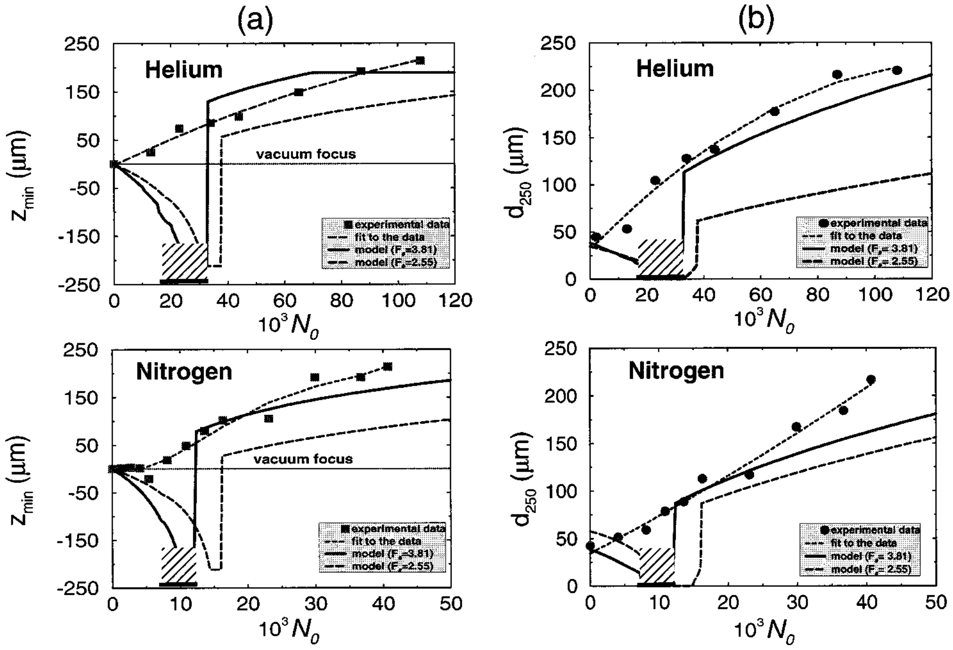

FIG. 15. (a) The location of the beam waist (minimum radius) and (b) of the beam diameter at 250 μm past the vacuum focus as a function of density. The points represent the experimental data obtained from records as those in Fig. 9 for nitrogen and in Fig. 10 for helium. The dashed line through the data points is a fit to guide the eye. The the prediction of the ray tracing model for the effective (solid line) and nominal (dashed line) $F_{\#}$ is also shown.

radiation all appear similar in form to those taken with nitrogen gas showing a uniform distribution of speckles. Again for all these gases, as seen from the shadowgrams, a few filamentary striations are observed to carry on beyond the end of main plasma. region. Overall these gases are demonstrating the domination of refractive defocusing at these high densities. Although not shown, at lower pressures their behavior was also qualitatively similar to nitrogen gas.

C. Time resolved shadowgraphy

Further information on the interaction process can be obtained from a time resolved shadowgram taken throughout the interaction period. Images taken at times of 0.0−2.0 ps are shown in Fig. 13 for nitrogen and hydrogen gas at relatively high atomic densities of $N_0 = 0.041$ and 0.16, respectively, which led to comparable electron densities in the peak ionization region. The starting time $t = 0.0$ ps is arbitrarily set to be the time at which the leading edge of the pulse arrives at the vacuum focal position. The sequence of images for nitrogen shows an orderly progression of refraction with the beam smoothly spreading out as it propagates forward. However, for hydrogen a significantly different pattern is observed. After arriving at the vacuum focus portion two prongs of light jut forward and the lateral spreading of the radiation appears constrained. This channeling of the propagation of the radiation is very similar to the transmitted images shown previously at 250 μm past focus. The transmitted image for the hydrogen gas image shown at $t = 1.33$ ps is shown in Fig. 14 together with the transmitted image for a similar nitrogen shot. The difference in both the shadowgrams and the transmitted spots is very apparent in this direct comparison. Considerable fine detailed modulation giving a feathery appearance in the shadowgram image is observed for hydrogen, which is not seen in the images for other gases. Also, in the shadowgrams of hydrogen fainter filaments can be seen branching out from the main plasma region. Over the next few picoseconds the ionization from these finer filaments increases and leads to the full image as observed at the late of $t = 9$ ps as shown Fig. 11.

D. Comparison with the ray tracing model

In this section we compare the experimental results with the predictions of the ray tracing model. There are some quantities whose variation with density conceivably can be compared and they have already been presented in Fig. 7 while their experimental value can be extracted from the information contained in Figs. 9–11. They are (a) the minimum radius exhibited during the interaction, (b) the location along the beam propagation of the waist, (c) the transmitted spot size at 250 μm past vacuum focus, and (d) the width of the Rayleigh zone. However, there is certain ambiguity associated with the experimental value of the minimum radius and Rayleigh zone width since the intensity of the 1ω and 2ω side-on images shown in Figs. 9–11 cannot be interpreted as being simply proportional to the locally prevailing laser intensity [42,13]. On the other hand, the measured spot size at 250 μm past vacuum focus and the location of the beam waist can be reliably obtained from the experimental data. The latter quantity is deduced from line outs of the 1ω records as the point where the maximum intensity occurs.

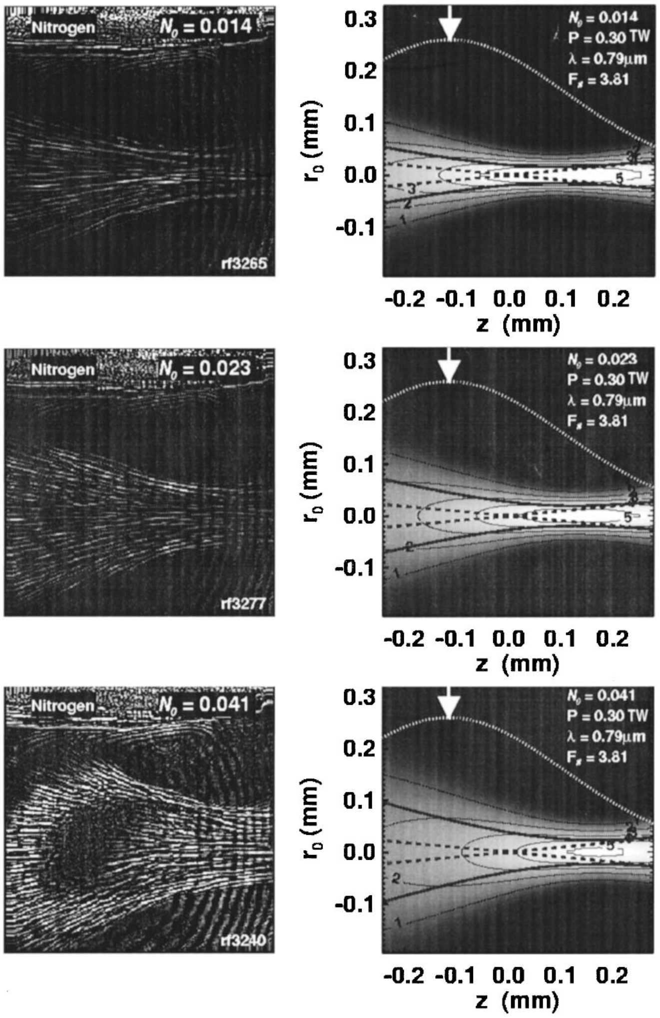

FIG. 16. Comparison of the experimentally obtained shadowgrams (left column) with the predictions of the ray tracing model (right column) for nitrogen and the indicated peak densities. In the experimental records the shadow of the gas jet orifice is visible in the upper part. In the model calculations the thick solid line represents the $1/e$ beam radius variation in the presence of the gas jet while the thick dashed line in vacuum. The ionization contours are given as labeled thin lines and the gray scale depicts the continues variation of the ionization degree up to its maximum value of $Z = 5$. The arrow gives the exact location of the peak density while the dotted line its variation along the z axis.

For the case of helium and nitrogen, this comparison is given in Fig. 15. In the discussion of Sec. IV A, it was pointed out that the vacuum spot profile deviates considerably from the ideal Gaussian beam profile assumed by the ray tracing model. To compensate for this deviation we have treated the $F_\#$ of the beam as a free parameter and we have varied it until the best fit to the experimental data was obtained. This procedure renders an effective F number of $F_\#^{\mathrm{eff}} = 3.81$, which is about 50% higher than its nominal value. This value would correspond more closely to the size of the high intensity structures observed in the non-uniform spatial profile of the laser beam. A more accurate analysis would involve higher modes of propagation in addition to the fundamental Gaussian mode, which in turn would increase the contribution of the diffraction spreading and would prevent self-focusing [39].

The resulting ray tracing predictions are then in good agreement with the experimental data in the density range where refraction is dominant. The predicted self-focusing for $N_0 \sim 0.025$ for helium and for $N_0 \sim 0.01$ for nitrogen was not observed experimentally. This can be explained on the basis of the form of the laser beam profile (see Fig. 8). The broader background peak reduces the maximum intensity that is required for the relativistic self-focusing and in addition smears out the image at 250 μm past vacuum focus. The interaction of the double Gaussian profile shown in Fig. 8(b) with the gas jet is quite complicated but it appears that the broader background pulse is responsible for the ionization defocusing observed even in the density range where self-focusing would be expected to occur.

A direct comparison of the shadowgrams with the ray tracing model is depicted in Fig. 16 for the case of nitrogen and for three densities in the refraction dominated region. The experimental records have been computer processed with a high-pass frequency filter to increase the contrast while the model results have been obtained for the same input parameters as in Fig 15. For the interpretation of the experimental results it is important to keep in mind that the experimental records are reversed, i.e., the dark regions are where the intensity of the 2ω probe light is the highest. Furthermore, the diffraction rings observed in the background are due to the probe beam and of no consequence to this discussion.

There are two features that are rather striking in the experimental records of Fig. 16. First is the sharp well defined boundaries of the shadow cast by the interaction region and second the fine structure in the form of regular striation of the shadow. The first feature is associated with the transition boundary between neutral gas and singly ionized nitrogen atoms. It indicates that even small intensity changes such as those existing in the wings of the radial beam profile result in substantial refraction index gradients and that these gradients are produced at well defined regions where the intensity first exceeds the value required for single ionization of the nitrogen atom (see Fig. 3). In this context, it is expected that the observed shadowgrams should correspond to the outer ionization contour, $Z=1$, predicted by the model. As can be seen the predicted refraction by the ray tracing model agrees qualitatively well with the images and it reproduces the overall behavior as the density increases.

The second feature has been previously observed in similar experiments and it has been attributed to the refractive splitting of intensity nonuniformities (hot spots) in the laser beam profile [46,47]. An original hot spot in the beam profile would refract faster than the rest of the beam due to the higher local electron density. This in turn would result in redistribution of intensity and in creation of regions with strong radial density profiles. The tendency is for light rays to be refracted out of high electron density regions and to be concentrated in regions of low ionization. These new regions of higher intensity would ionize more strongly again and cause the light to refract out of these new regions as it propagates forward. Therefore, an initial hot spot would multiply several times after passing through the interaction region. There are two arguments that support this conjecture. The first is based on an estimate of the path length that is required for a spot with a minimum radius $r_{\rm hs,min}$ to expand via refraction to a radius $r_{\rm hs}$. This can be obtained from the integration of Eq. (3.12) in which only the refractive term is considered (see also [41,48]):

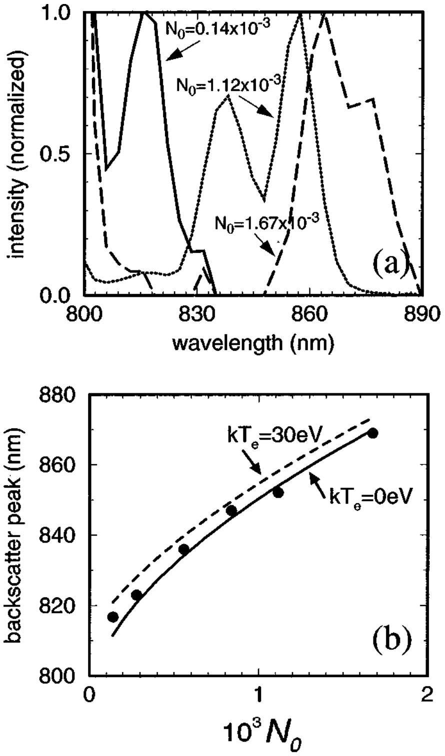

FIG. 17. (a) Typical Raman backscattered spectra from static-filled N_2 gas (normalized to the peak Raman signal). (b) The wavelength of the peak Raman backscattered signal vs atomic gas density (normalized to n_c). The lines in (b) give the theoretical estimate using the SRS frequency matching condition for two temperatures of 0 eV and 30 eV. Each data point represents the average of a number of shots and shot-to-shot variations are within $\pm 1\%$.

$$\Delta z = z - z_{\min} = \frac{1}{\sqrt{q_0 N (P/\pi)^{1/(4\alpha-2)} \kappa_0}} \times \int_{r_{\rm hs,min}}^{r_{\rm hs}} \left(\frac{1}{r_{\rm hs,min}^{1/(2\alpha-1)}} - \frac{1}{r^{1/(2\alpha-1)}} \right)^{-1/2} dr. \qquad (4.1)$$

For small relative radial expansion $\Delta r_{\rm hs} = r_{\rm hs} - r_{\rm min,hs}$, the integral in Eq. (4.1) can be approximated as $\Delta z \approx r_{\rm hs}^{\alpha/(2\alpha-1)} \sqrt{\Delta r_{\rm hs}} / [q_0 N (P/\pi)^{1/(4\alpha-2)} \kappa_0/(2\alpha-1)]^{1/2}$. The distance necessary for a hot spot to double its size, i.e., $\Delta r_{\rm hs} \approx r_{\rm min,hs}$ corresponds to the beam path necessary for the initial hot spot to split into two filaments. From Eq. (4.1) it is seen that this distance scales with the density as $\Delta z \sim 1/\sqrt{N}$. For the case of nitrogen, $P=0.1$ TW and an initial hot spot having $r_{\rm min,hs} \approx 10$ μm this estimate gives as a splitting distance $\Delta z \approx 187$ μm for $N=0.001$, while the same distance is $\Delta z \approx 60$ μm for $N=0.01$. In both cases the splitting distance is considerably smaller than the actual spatial extent of the gas volume (>500 μm) through which the beam propagates. Therefore, even for the lowest peak densities used in the experiment, a hot spot would split into two several times.

The second evidence for the multirefractive splitting of the hot spots in the beam profile can be found in the experi-

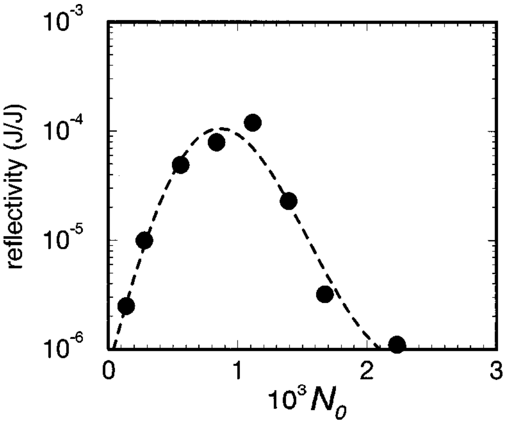

FIG. 18. The reflectivity of the Raman backscattered light (810–1130 nm) vs gas pressure for static filled nitrogen gas. Shot-to-shot variations are ±50%.

mental records of the transmitted spot at 250 μm past focus given in the second row of the Figs. 9–11. In the case of helium and nitrogen the records show a number of hot spots uniformly distributed in the radial direction while for hydrogen the high intensity spots remained localized at a position that is determined by the initial focal spot imprint (see Fig. 8). This indicates that when the refraction is dominant as in the case of helium and nitrogen, splitting of the hot spots occurs with the consequence of creating beamlets that on the shadowgrams of Fig. 16 look like filaments.

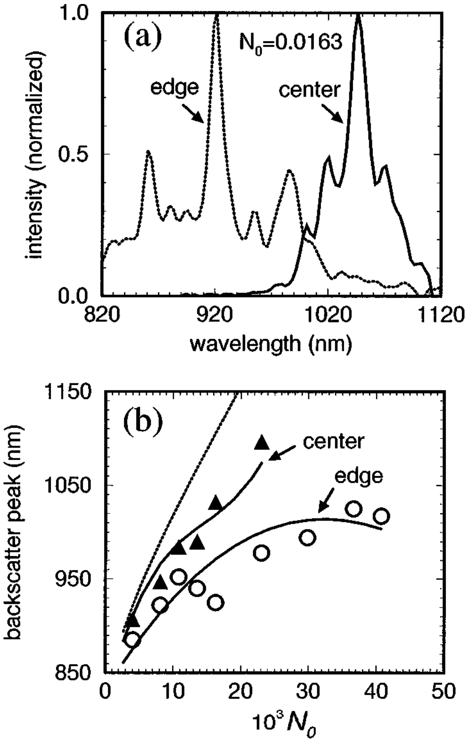

FIG. 19. (a) Typical Raman backscattered spectra (normalized to the peak Raman signal) for a nitrogen gas jet. (b) The wavelength of the peak Raman backscattered signal vs peak nitrogen gas jet atomic density. The solid lines in (b) give theoretical estimates of the expected wavelength given the He-like ionization stage and the observed position of peak intensity from Fig. 9 and similar data for focusing at the edge of the gas jet. Shot-to-shot variations are ±2%. The dotted line gives the expected shift if the peak focus remained at the vacuum focal position for the center focus position.

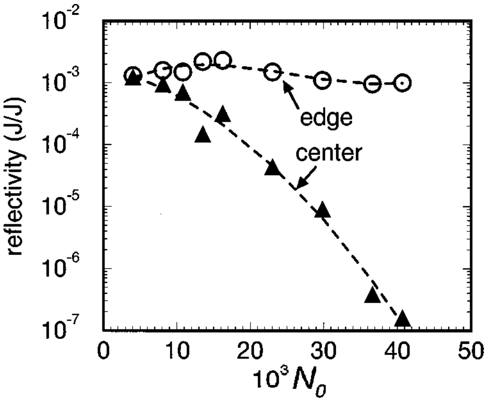

FIG. 20. The reflectivity of the Raman backscattered light (820–1130 nm) for a nitrogen gas jet vs atomic density. Shot-to-shot variations are ±50%.

E. Raman scattering

1. Raman back scattering in static-filled N_2 gas

Low pressure static-filled nitrogen was used to observe the relation between Raman backscattered spectra and the gas parameters. The tunnel ionization model [17] predicts that in the present laser condition, the He-like ionization state can be reached for nitrogen for intensities of $>2\times10^{16}$ W/cm^2. Thus the electron density and plasma frequency can be deduced directly from the static gas pressure. Figure 17 gives the wavelength of the peak signal measured from the backscattered spectra versus gas pressure. It is found that the peak position of the downshifted Raman spectra is consistent with the theoretical frequency matching condition [49]:

$$\omega_s = \omega_L - \omega_p \tag{4.2}$$

in which ω_L, ω_p, ω_s are the frequencies, respectively, of the laser, the electron plasma wave, and the backscattered light. In the case of low plasma densities compared to critical density for which $\omega_p \ll \omega_L$, the plasma frequency is given by $\omega_p = \omega_{p0}\sqrt{1+12\omega_L^2 kT_0/(\omega_{p0}^2 m_e c^2)}$ where ω_{p0} is the cold plasma frequency and T_0 is the plasma temperature. In Fig. 17(b) two curves are shown corresponding to plasma temperatures of 0 and 30 eV. It can be seen that the averaged data agree with a relatively cold plasma at 0–30 eV indicating that there is little heating of the plasma in the longitudinal direction for this low density range. These results are similar to those previously reported by Perry *et al.* [50] who also confirmed the agreement between observed shift and expected plasma density. Individual shots can show spectral features with slightly larger shifts such as the shoulder at ≈875 nm for the highest density spectrum shown in Fig. 17(a). This shoulder would correspond to a temperature of ≈46 eV, indicating that perhaps late in the pulse more heating has occurred and late time backscatter would have a larger spectral shift.

The time-integrated reflectivity of the Raman backscattered light, defined as the ratio of backscattered energy integrated from 810 to 1130 nm to incident laser energy, is

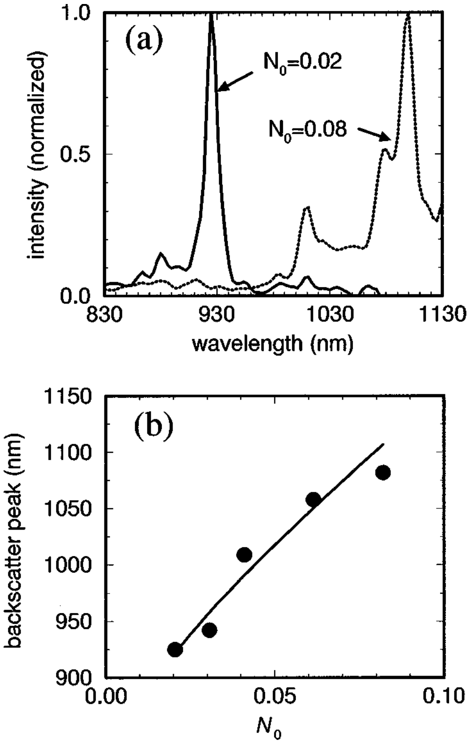

FIG. 21. (a) Typical Raman backscattered spectrum (normalized to Raman peak signal) for hydrogen vs gas density. The spectrum is corrected for the spectrometer response and filter transmission functions. (b) The wavelength of the peak Raman backscattered signal vs peak gas jet atomic density. The line gives the theoretical estimate using the SRS frequency matching conditions, for which the electron density is determined with the relation described in the text. Shot-to-shot variations are ±2%.

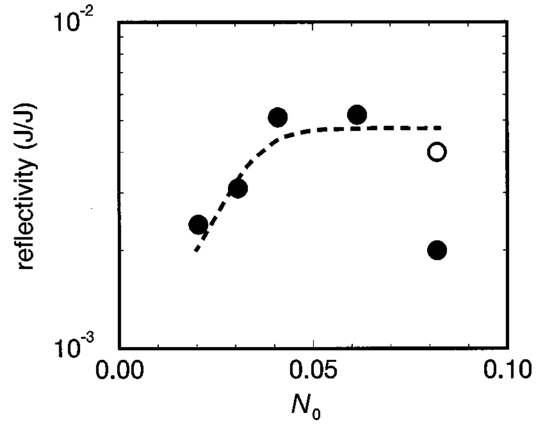

FIG. 22. The reflectivity of the Raman backscattered light (830−1130 nm) vs peak atomic density for a hydrogen gas jet. Error bars indicate shot-to-shot variations. The measured point at atomic density of $N_0=0.08$ is underestimated due to the limited wavelength range of the spectrometer. Assuming that half the spectral energy is cut off one can estimate the reflectivity as double the measured value (open point and dashed curve).

shown in Fig. 18. It is found that the reflectivity increases with pressure, reaches a maximum at about $N=0.001$, and then decreases at higher pressures. A similar result was found by Malka *et al.* [29] when helium was used. The trend of decreasing reflectivity versus gas pressure at atomic densities of $N \geqslant 0.001$ indicates that ionization-induced refraction plays a significant role in decreasing the peak intensity as discussed in [29]. The result agrees with the onset of refraction above $N \approx 0.001$ as shown in Fig. 5.

In addition to the nominal case of linearly polarized laser for the experiment, we also investigated the case of elliptically polarized laser light ($E_x:E_y=1:2$) in the Raman backscattering experiment. We did not observe any significant change of the wavelength of the peak Raman signal between the elliptical- and the linear-polarization cases, which means that for the present condition, even with elliptically polarized light for which significantly more above threshold ionization heating is expected [51] no strong heating is observed in the longitudinal direction.

2. Raman back scattering in N_2 gas jet target

Measurements of Raman backscatter were also carried out in the gas jet target. Figure 19 gives the peak wavelength of the downshifted spectra versus gas jet peak atomic density. In the plot we also give a theoretical estimate of the peak wavelength corresponding to the estimated electron densities based on the location of the peak intensity as observed from the 1ω self-emission [see Fig. 9 and Fig. 15(a)]. It is found that the measured peak position is consistent with theoretical estimate that the nitrogen ionization stage is in He-like ions for the position in the gas jet where the peak intensity occurs.

We also focused the laser at the edge of the gas jet, i.e., at a distance $z_{\mathrm{jet}}=315$ μm from the jet axis instead of $z_{\mathrm{jet}}=115$ μm, which is designated as center focused. The Raman backscatter signal is still visible for much higher peak atomic densities. The observed peak wavelengths of the Stokes shifted backscattered signal are also plotted as a function of peak atomic density in Fig. 19. In this case the scattered light signal is still strong at high pressures, while very weak if the laser was focused at the center of the gas jet. The expected peak wavelength based on the electron densities at the location of peak intensity also are plotted in the figure. Within the experimental error the observed shifts agree with the predicted shifts confirming that the peak intensity region is moving toward the incident laser as predicted. Near $N_0=0.016$, the spectra showed some modulations. The modulations also lead to some scatter in the data depending on which peak is the strongest and thus leads to the scatter in Fig. 19(b). Figure 20 gives the reflectivity measurement of

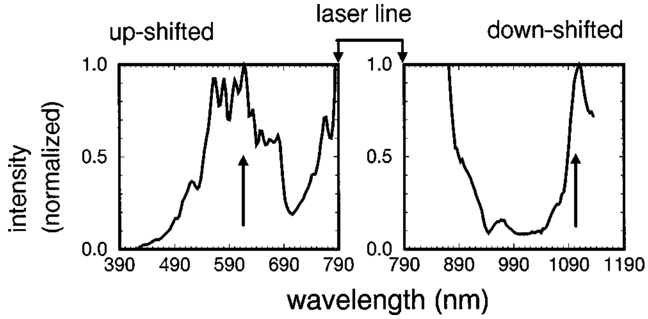

FIG. 23. Typical Raman forward scattered spectra for hydrogen gas at atomic density $N_0=0.08$. In the downshifted (upshifted) spectra, arrows indicate the expected peak position of the first Stokes (anti-Stokes) light theoretically determined by frequency-matching condition.

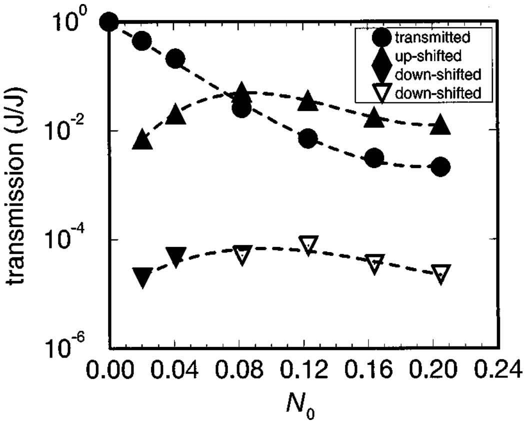

FIG. 24. The fraction of the transmitted light (760–820 nm), forward scattered downshifted (830–1130 nm) and upshifted (400–750 nm) light relative to the incident laser energy within an $F/57$ cone angle for hydrogen gas. For down-shifted spectra, values with $N_0 > 0.04$ are underestimated (open triangles pointing down) due to the limited spectral range of the spectrometer. Shot-to-shot variations are ±20%.

the scattered light. It is seen that at high pressures, the scattered light signal focused at the edge is more intense than that in the case of laser focused at the gas jet center. This means that in the case of the laser focus at the gas jet edge the refraction defocusing, although reduced partially, still plays a major role for the experimental parameters here.

3. Raman scattering in H_2 gas jet target

Raman backscatter was also measured for a hydrogen gas jet. Hydrogen has only one ionization stage and is expected to be fully ionized in the peak intensity interaction region. Figure 21(b) gives typical Raman backscattered spectra and the wavelength of the peak signal measured from the Raman backscatter spectra versus the peak gas target density. The results reveal that the measured position is consistent with the theoretical estimates of the frequency matching condition in Eq. (4.2). As has also been found by others [52,53], we find that the Raman backscattered spectra are broadened and there are modulations [54], as shown in Fig. 21(a). These modulations disappear at lower intensity (~1/3 of the laser energy used here) in which case the backscattered Raman spectra show only a single peak as usually observed in low intensity or low density Raman spectra [50]. The explanation of the broadening and modulation of the spectra is not clear yet, but may be concerned with the strongly coupled nature of the Raman backscattering [52] in our conditions, wave breaking [30,31] and the temporal bursting of the backscatter [55].

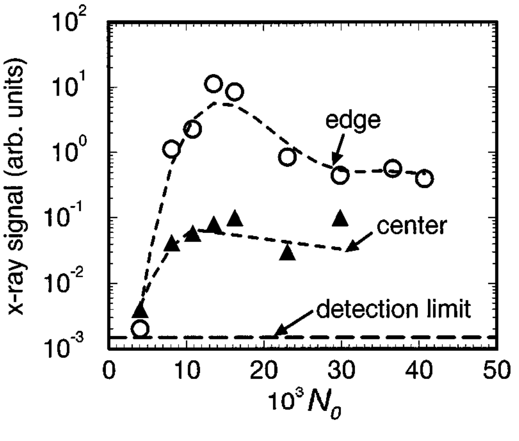

FIG. 25. Hard x-ray emission through a 150 μm thick aluminum filter (>8 keV) vs atomic density for a nitrogen gas jet. The detection limit is limited by the oscilloscope. Shot-to-shot variations are ±50%.

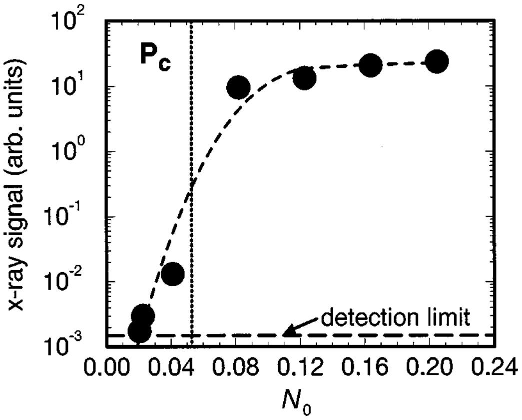

FIG. 26. Hard x-ray emission through a 550 μ m thick aluminum filter (>12 keV) vs peak plasma density for a hydrogen gas jet. The dashed line gives the threshold for the critical power $P_c = 16.2 n_c / n_e$ [GW], where $P_c = 0.3$ TW is the laser power on the target. The detection limit (long dashed line) is limited by the sensitivity of the oscilloscope. Shot-to-shot variations are ±50%.

The reflectivity of the Raman backscattered light, which gives the level of the backscattered light to the incident laser is plotted in Fig. 22. For the data point at $N_0 = 0.08$, the limited wavelength range of the spectrometer truncates almost half the spectrum, which leads to an underestimation of the energy of the Raman scattering. However, even assuming that the reflectivity at this density region should be twice the measured value, the results show that the backscatter signal saturates at atomic densities greater than 0.04.

A series of measurements were also made for the Raman forward scattering and part of the spectrum is shown in Fig. 23, which has been corrected for the transmission of filters and the response of the spectrometer. We observed evidence of both frequency downshifted and upshifted spectra. In the forward scatter signal the upshifted spectrum is much stronger than the downshifted spectrum. This is in contrast to the measurements of the backscattered spectra. The peak position of the downshifted spectra is consistent with theoretical estimates as was the case for the backscattered signal. The upshifted spectra show a broad, somewhat modulated continuum of radiation centered around the expected anti-Stokes wavelength. This is in contrast to the results reported in [28] where a clear peak was observed corresponding to the expected anti-Stokes wavelength. However, the latter report was for a density of $0.02 n_c$ and higher power and/or intensity as compared to Fig. 23, which is for a peak density of $0.2 n_c$. It is plausible that the anti-Stokes light is seeded by a very strong broadband background, which may stem from ionization induced spectral blueshifting [56] or the plasma wakefield noise spectrum [57,58].

We estimated the fraction of both upshifted (from 400 to 750 nm) and downshifted (from 830 to 1130 nm) scattered light relative to the incident laser energy, as shown in Fig. 24(b). (We should point out that for densities greater than $N_0=0.08$, the values for the downshifted scattered light are underestimated due to the limited range of the spectrometer.) The measurements reveal that the scattered light increases and then around $N_0=0.08$ decreases slowly as pressure increases. They also show that the fraction of the upshifted light is two orders of magnitude higher than that of the downshifted light.

F. Hard x-ray measurements from H_2 and N_2 gas jet targets

During the Raman scattering measurement, we also measured hard x-ray emission from the laser gas interactions. Figure 25 gives results for N_2 for the two positions of the focus relative to the gas jet center when a 150 μm thick aluminum filter was used. One sees that when the laser is focused at the edge of the gas jet, the x-ray signal is stronger than when focused in the middle of the gas jet. A relative peak was observed for $N_0 \approx 0.015$ for the case of focusing at the edge. At high pressures, refraction plays a dominant role, and laser intensity decreases, which also produces lower x-ray signals. For the case of laser focus at center, the x-ray signal is weak and in this case the Raman scatter is also weak as seen in Fig. 20. This correlation implies that the x-ray emission may be caused by the electrons that are heated by the Raman process. When a 550 μm Al filter was used the x-ray signals were much weaker by about one order of magnitude.

In contrast, very strong x-ray emission and different features were observed in hydrogen, as shown in Fig. 26. In this case a 550 μm aluminum filter was used. A distinct feature is that the x-ray signal increases rapidly with pressure and then ''saturates'' at higher pressures. The mechanism for the production of the strong hard x rays is not clear since unlike nitrogen gas there should be no significant keV x-ray emission from the hydrogen gas itself. But it is expected to be related to the impact of fast electrons on the metal edge of the gas jet. In the plot, we also give the position for the onset of the relativistic self-focusing as given by relation $P_c=16.2 n_c/n_e$ [GW] . The most interesting result is that the onset of a high level of hard X-ray emission is consistent with the threshold for the onset of relativistic self-focusing, which may indicate an experimental correlation between the two phenomena.

V. DISCUSSION

The laser propagation model given earlier has already been compared to experimental results as given in the previous sections. This model employs a number of simplifying assumptions in order to allow for simple analytical limits to be derived and simple numerical solutions to be worked out. A key assumption is that the intensity profile corresponds to an ideal laser Gaussian beam. One of the key results of the model is the prediction of both a lower and an upper density cutoff limit, i.e., a density window, for which relativistic self-focusing can occur as given by Eq. (3.19) for the upper density and the normal density limit quoted for the critical power for relativistic self-focusing for the lower density. The lower density limit is given by the balance between diffraction and the self-focusing term while the upper limit is given by the balance between the refraction and self-focusing term. This window of allowed self-focusing still has a critical power threshold in order that self-focusing occurs at all.

The comparison of the model with the observed behavior in helium and nitrogen shows that in the high pressure limit both the predicted refraction spreading and the position of the peak intensity region for the beam are in reasonable agreement with the experimental observations, as shown in Fig. 15. The position of the maximum intensity region is also consistent with the measured Raman shifts in the backscattered radiation from the nitrogen gas jet. The fact that the beam size, measured 250 μm past focus, at the highest pressures for nitrogen is slightly larger than predicted may be explained in part by the increased refraction observed for the part of the beam closest to the gas jet nozzle. This is due to the fact that the gas density is significantly higher as one approaches the nozzle. However, for all the gases except hydrogen we did not observe the predicted window of relativistic self-focusing. This is most likely due to the fact that our laser beam was far from an ideal Gaussian and was better represented as the combination of two Gaussians, one a few times diffraction limited and the other several times diffraction limited as shown in Fig. 8. This beam profile indicates that we have a combination of numerous higher order modes that will lead to a much larger contribution to the diffraction term than we have used in our model. Thus the lower density boundary for relativistic self-focusing given by the balance between diffraction and the self-focusing term will be increased by a significant amount. Since the power that we have in the laser is only 0.3 TW a significant change in this boundary would eliminate the window for self-focusing that appears to be the case from the experimental results. It would require further experiments with much better beam profiles in order to quantitatively confirm the prediction of the model in this sensitive region.

The shadowgrams also indicate significant absorption of the propagating laser light at the higher pressures measured. This is evidenced by the fact that the intensity falls below that required to ionize the gases to the first ionization stage before propagating through the gas jet. The model calculations show that without absorption there should be sufficient intensity to ionize throughout the full interaction region. The absorption was also evident in the reduced transmission observed in the camera viewing the transmitted radiation. The same truncation of ionization was observed for all the gases except hydrogen as shown in Fig. 11. The expected absorption can be estimated in the region of low ionization where the intensity is also weak by calculating the inverse bremsstrahlung absorption length [e.g., Eq. (1) from Ref. [24]. For $n_e=0.04 n_c, T_e=3$ eV, $Z=1$, and $\ln\Lambda=3$ one would estimate an e-folding absorption length of 62 μm at 790 nm and 247 μm at 395 nm. The second absorption length would agree with the observed absorption of the 2ω probe beam in the high density shadowgrams, e.g., $N_0=0.041$ for nitrogen as shown in Fig. 9 where substantial absorption is observed for a plasma region of ≈ 300 μm in diameter. For the main laser pulse at 1ω the absorption coefficient is reduced because the oscillatory velocity $v_{\rm osc}=eE/\omega m_e$ is much higher than the thermal velocity, $v_{\rm th}=\sqrt{kT_e/m_e}$ [59,60]. For an intensity of 10^{15} W cm^{-2} the ratio is $v_{\rm osc}/v_{\rm th}=4.4$ for an estimated plasma temperature of 3 eV. This would lead to a tenfold increase in the absorption length at 1ω giving an absorption length of ≈ 620 μm. However, as the beam diverges and the intensity drops to $I=2\times 10^{14}$ W cm^{-2} that of the first ionization threshold for nitrogen the ratio $v_{\rm osc}/v_{\rm th}$ drops to 2, leading to an absorption length of 134 μm. While these values are only estimates of the plasma conditions, one can see that it is reasonable that the there can be significant absorption of the main beam in the tail of the plasma and thus result in the observed truncation of the plasma region prior to the end of the gas jet target.

Another factor in the absorption is the observed large component of blueshifted light. In part this appears to be forward Raman amplification of blueshifted radiation from the ionization blueshift and perhaps wake field enhanced plasma wave noise.

The observation of filamentary structure in the outer regions of the plasma profile is consistent with a refractive propagation instability leading to a continuously evolving filamentation pattern. As discussed in Sec. IV D the estimated scale lengths for each filament range from 187 μm to 60 μm for densities of $N=0.001$ to $N=0.1$ in approximate agreement with structures observed on the images. Such a mechanism and similar estimate of structure length were given in a previous publication by Denavit *et al.* [48]. Similar structures were also observed in shadowgrams reported for 1 μm laser interactions by Mackinnon *et al.* [47]. In addition to the filamentary structures there are ringlike fringes in the high density regions of the shadowgrams as can be seen in in the highest density shadowgram for helium shown in Fig. 10. These rings could be an artifact due to the refraction of the probe beam rays through the electron density profile. Since the imaging system maps all the rays back to the image plane, those rays that are significantly bent in traveling through the plasma will be mapped onto an incorrect position in the image plane and lead to interference with those rays that have been less bent and mapped onto the same point in the image. The optical path lengths integrated through the plasma will be different for these rays, which can lead to constructive or destructive interference. Since the degree of bending varies from none to maximum to none again as one traverses from the center of the plasma to beyond the edge of the plasma, the resulting increase and subsequent decrease in phase shifts will lead to dark and light interference bands. These bands are distinctly different from the long filamentary structures and thus we believe the latter are truly indicative of beam filamentation. This is borne out by the fact that images of transmitted radiation show a very smooth distribution of filamentary spots when viewed 250 μm past the focal position.

A number of results from the stimulated Raman forward and backscatter measurements help to reinforce the predictions of the propagation model. The measured spectral shifts in the nitrogen gas jet target agree with the calculated shifts taking into account the motion of the peak intensity region and ionization state of 5^+. The ionization state indicates that in all cases up to $N_0=0.02$, while the intensity is reduced due to refraction, as shown in Fig. 16 there is always a a region with an intensity of greater than 2×10^{16} W cm^{-2} as predicted by the model. For the static gas case the increase and subsequent decrease of peak backscattered Raman signal corresponds to the expected effect of increasing signal with density combined with a reduction of intensity as the background density is increased. Similar observations have been made by Malka *et al.* [29] for helium gas.

Finally, the fact that all the spectral shifts for both the static gas and the gas jet cases agree well with the expected cold electron plasma dispersion relation leads to the conclusion that the longitudinal plasma temperature is very low, less than on the order of 30 eV for the case of the backscatter from static nitrogen for atomic densities of $N_0<0.002$ as shown in Fig. 17. Heating in this case would come both from residual energy remaining in the electrons from the tunnel ionization process and the inverse bremsstrahlung heating reduced by the strong field correction [59,60]. Typically the residual heating for tunnel ionization can be estimated to be on the order of 0.1 times the ponderomotive energy of the ionizing field at the time of electron production [4]. The first few electrons are ionized at low intensities and thus have little residual heating while the final electrons are generated at higher field strengths and thus with higher residual energies. Using the estimate that the temperature is 1/10 of the ponderomotive energy and averaging over the energies of all five electrons for nitrogen yields a residual temperature of 30 eV for the electrons after ionization. However, this temperature is in the transverse direction. Because of the low collisionality of the plasma the transfer of momentum and energy to the longitudinal direction where it could influence the electron plasma waves associated with the forward and backward Raman scattering will take longer than the laser pulse duration and thus reduce the effect of this temperature on the observed Raman spectra. More important is the inverse bremsstrahlung heating. Assuming an estimated plasma temperature of 30 eV the strong field correction factor [59] reduces the absorption of high intensities in the range of $1\times 10^{16}-1\times 10^{17}$ W cm^{-2} to an effective intensity of 1×10^{15} W cm^{-2}. The heating due to this effective intensity in fully ionized nitrogen can be calculated for the peak of the laser pulse, at $\tau=125$ fs, from Eq. (3) of Ref. [9] (corrected for a missing factor of 2/3) yielding a temperature of 39 eV for an atomic density of $N_0=0.001$ and 98 eV for $N_0=0.01$. The fact that the observed shifts for the static fill case corresponding to the lower density value given here, indicated temperatures of less than 30 eV would tend to indicate that the strong field correction is probably greater than estimated here (i.e., the starting temperature is significantly less than 30 eV). Some features in the spectra indicate temperatures of over 30 eV which would probably indicate Raman backscatter later in the pulse. The higher density estimate is more appropriate for the gas jet target shots. A temperature of 98 eV would correspond to an increase in spectral shift of approximately 10 nm. This is approximately the uncertainty due to the uncertainty of the gas density and the exact location in the gas jet where the backscatter occurs. Thus heating to the order of 100 eV would be within the error bars of the measured spectral shifts given the shot-to-shot fluctuations and uncertainty in the exact density of the interaction region. Significantly larger heating rates would be discrepant with the data and thus this is a strong indication of the effectiveness of the strong field correction in reducing the inverse bremsstrahlung heating rate.

The behavior of the propagation of the femtosecond pulse in high pressure hydrogen was significantly different from that in other gases with a number of the diagnostics indicating behavior at the threshold for relativistic self-focusing. These included the time resolved shadowgrams taken throughout the interaction period showing the forward propagation of plasma channels, the corresponding transmitted radiation images showing the development of hot spots at the position 250 μm past the vacuum focal position and the appearance of a strong x-ray signal with photon energies above 12 keV for densities above that required to reach the critical density for relativistic self-focusing. The apparent saturation of the x-ray signal with pressure may just be an artifact of the thin scintillator used in the detector that would allow higher energy x-rays to transmit through the detector, giving a decreasing signal response with x-ray photon energy above 20 keV. The data from the 1ω images for hydrogen show an increasing diffuse emission region at higher pressures. It may be that, as argued by Monot *et al.* [13] and Chiron *et al.* [61], as self-focusing occurs and the laser beam propagation is confined to a density channel with reduced electron density the amount of Thomson scattering decreases and thus one would not see clear images of the higher intensity channel regions. The 2ω images show a different picture of the interaction. In this case, a narrow single channel is observed even at very high pressures. This may indicate that there is one dominant high intensity channel near the central axis of the laser but that this splits into a few weaker channels which are subsequently observed in the transmitted images 250 μm past the vacuum focal position.

The hard x-ray signals observed for hydrogen gas jet targets at the higher densities presumably come from fast electrons impacting on the metal gas jet nozzle. High amplitude plasma oscillations that in the present experiment can be caused by the Raman forward scattering process and large wake fields that may be generated by self-modulation of the laser pulse can be excited during laser propagation. Electrons from the background plasma can be trapped and accelerated by these plasma waves due to wave breaking. We find in the saturation region of Fig. 26 for lower laser energy shots, the x-ray signal decreases dramatically. This indicates a tight correlation between the Raman forward scattering and hard x-ray generation, i.e., strong x-ray signal is accompanied by enhanced Raman forward scattering. The determination of the mechanisms for the generation of high energy electrons would require a dedicated experiment to characterize the fast electrons in detail.

VI. CONCLUSIONS

A study has been carried out on the propagation of high power Ti:sapphire laser pulses in high density gas targets. In contrast to previous investigations, we have focused our interest in the density range around $0.1n_c$ or $n_e \sim 10^{20}$ cm^{-3} for which the threshold for relativistic self-focusing could be achieved for modest intensities of a fraction of a terawatt. In this regime the refraction due to the nonuniform ionization profile of the gas competes with the relativistic self-focusing process. This competition was studied with a simple Gaussian beam analytic model which identified the density regime and intensity regime for which relativistic self-focusing could be expected for given gases. Both an upper density limited by diffraction and lower density limited by power were identified in the result. While a window of relativistic self-focusing was predicted for nitrogen gas for our experimentally available power of 0.3 TW, this was not observed in the experiments. Instead, a steady onset of refraction was measured as a function of gas density in reasonable agreement with the model prediction at high densities. This onset of refraction was observed also in helium and in all the higher atomic number gases. It is expected that the poor beam quality, a fraction of which was a few times diffraction limited and the majority of which was several times diffraction limited prevented the high intensities from being achieved which would lead to self-focusing before the refraction effect set in. It would be necessary to repeat the present experiments with much higher beam quality in order to verify the predicted window of self-focusing.

In the case of hydrogen gas for which refraction would have the least effect for all the gases, clear evidence for the onset of self-focusing was observed in three of the diagnostic measurements. In the time resolved shadowgraphy channeling structures were observed in the leading part of the laser pulse in clear contrast to the smooth refraction behavior observed in for all the other gases studied. The transmitted radiation at a position 250 μm past focus showed clear signs of high intensity channels again in clear contrast to the diffuse scattering observed for all the other gases. Finally, hard x-ray emission, presumably from the fast electrons, generated by the relativistically driven plasma, impacting the gas jet nozzle, was observed for densities exceeding those required for the threshold for relativistic self-focusing.

Raman backscattered spectra in nitrogen provided additional supporting data on the predicted refraction and self-focusing behavior of the gases. For the case of the gas jet interactions the spectral shifts indicated densities in agreement with those at the position of the highest intensity point in the gas jet profile. For the static fill cases the spectral shifts agreed with those of a relatively cold plasma with a temperature of less than 30 eV. For the gas jet cases the error bars and uncertainty in experimental parameters would allow temperatures of up to 100 eV. Such cold temperatures would be in agreement with the expected 30 eV heating due to tunnel ionization for nitrogen and a small amount of inverse bremsstrahlung heating, which is significantly reduced by the strong field correction due to the large ratio of $v_{\mathrm{osc}}/v_{\mathrm{th}}$. The fact that significantly higher temperatures were not observed confirms the expected reduction in inverse bremsstrahlung expected for such strong laser fields.

The reduction of Raman backscatter observed for atomic densities above $N_0 = 0.001$ of static filled nitrogen and for densities above $N_0 = 0.015$ for nitrogen gas jets both are in agreement with the reduction in intensity expected due to the refraction in the ionized gas. At high densities the Raman backscatter saturates. For hydrogen gas jets the Stokes component of forward stimulated Raman scattering was observed. However, an even stronger upshifted component of the scattered spectra was observed, which cannot be simply attributed to anti-Stokes Raman light. This upshifted component may stem from the ionization induced blueshifting of the main pulse combined with Raman amplification of plasma wake field noise induced signal.

Overall, it is clear that for electron densities of the order of $0.1n_c$ refraction plays a major role in controlling the interaction of the laser pulse with gas jet targets, particularly in the case of poor beam quality as in the present experiment. It is predicted and yet to be verified experimentally that there is window of density for which self-focusing should be observed for high densities of gases such as nitrogen but that a high quality beam, close to lowest order Gaussian mode, will be required in order to observe this result. For hydrogen the reduced ionization threshold allows the observation of the onset of relativistic self-focusing at the high density of $0.1n_c$ even in the presence of the the poor beam profile. This the first reported experimental evidence for the onset of relativistic self-focusing in a gas jet target with a high electron density of $n_e = 0.1n_c$.

ACKNOWLEDGMENTS

This work was funded in part by the commission of the European Communities in the framework of the Euratom-IPP association. X. Wang was supported by Max-Planck-Gesellschaft and the Chinese Academy of Sciences; he would also like to thank K. Eidmann for his help.

[1] T. Tajima and J. M. Dawson, Phys. Rev. Lett. **43**, 267 (1979).
[2] P. Sprangle, E. Esarey, A. Ting, and G. Joyce, Appl. Phys. Lett. **53**, 2146 (1988).
[3] K. Nakajima, D. Fisher, T. Kawakubo, H. Nakanishi, A. Ogata, Y. Kato, Y. Kitagawa, R. Kodama, K. Mima, H. Shiraga, K. Suzuki, K. Yamakawa, T. Zhang, Y. Sakawa, T. Shoji, Y. Nishida, N. Yugami, M. Downer, and T. Tajima, Phys. Rev. Lett. **74**, 4428 (1995).
[4] N. H. Burnett and P. B. Corkum, J. Opt. Soc. Am. B **6**, 1195 (1989).
[5] N. H. Burnett and G. D. Enright, J. Quantum Electron. **26**, 1195 (1990).
[6] P. Amendt, D. C. Eder, and S. C. Wilks, Phys. Rev. Lett. **66**, 2589 (1991).
[7] D. C. Eder, P. Amendt, and S. C. Wilks, Phys. Rev. A **45**, 6761 (1992).
[8] M. Tabak, J. Hammer, M. E. Glinsky, W. L. Kruer, S. C. Wilks, J. Woodworth, E. M. Campbell, and M. D. Perry, Phys. Plasmas **1**, 1626 (1994).
[9] C. E. Max, J. Arons, and A. B. Langdon, Phys. Rev. Lett. **33**, 209 (1974).
[10] J. C. Solem, T. S. Luk, K. Boyer, and C. K. Rhodes, IEEE J. Quantum Electron. **25**, 2423 (1989).
[11] G.-Z. Sun, E. Ott, Y. C. Lee, and P. Guzdar, Phys. Fluids **30**, 526 (1987).
[12] A. B. Borisov, A. V. Borovskiy, V. V. Korobkin, A. M. Prokhorov, O. B. Shiryaev, X. M. Shi, T. S. Luk, A. McPherson, J. C. Solem, K. Boyer, and C. K. Rhodes, Phys. Rev. Lett. **68**, 2309 (1992).
[13] P. Monot, T. Auguste, P. Gibbon, F. Jakober, G. Mainfray, A. Dulieu, M. Louis-Jacquet, G. Malka, and J. L. Miquel, Phys. Rev. Lett. **74**, 2953 (1995).
[14] R. Wagner, S.-Y. Chen, A. Maksimchuk, and D. Umstadter, Phys. Rev. Lett. **78**, 3125 (1997).
[15] A. Pukhov and J. Meyer-ter-Vehn, Phys. Rev. Lett. **76**, 3975 (1996).
[16] L. V. Keldysh, Sov. Phys. JETP **20**, 1307 (1965).
[17] M. V. Ammosov, N. B. Delone, and V. P. Kraǐnov, Sov. Phys. JETP **64**, 1191 (1986).
[18] P. S. Augst, D. Strickland, D. D. Meyerhofer, S. L. Chin, and J. H. Eberly, Phys. Rev. Lett. **63**, 2212 (1989).
[19] R. Rankin, C. E. Capjack, N. H. Burnett, and P. B. Corkum, Opt. Lett. **16**, 835 (1991).
[20] S. C. Rae, Opt. Commun. **97**, 25 (1993).
[21] E. E. Fill J. Opt. Soc. Am. B **11**, 2214 (1994).
[22] W. P. Leemans, C. E. Clayton, W. B. Mori, K. A. Marsh, P. K. Kaw, A. Dyson, and C. Joshi, Phys. Rev. A **46**, 1091 (1992).
[23] P. Monot, T. Auguste, L. A. Lompré, G. Mainfray, and C. Manus, J. Opt. Soc. Am. B **9**, 1579 (1992).
[24] Y. M. Li, J. N. Broughton, R. Fedosejevs, and T. Tomie, Opt. Commun. **93**, 366 (1992).
[25] C. G. Durfee III and H. M. Milchberg, Phys. Rev. Lett. **71**, 2409 (1993).
[26] P. E. Young and P. R. Bolton, Phys. Rev. Lett. **77**, 4556 (1996).
[27] M. Borghesi, A. J. MacKinnon, L. Barringer, R. Gaillard, L. A. Gizzi, C. Meyer, and O. Willi, Phys. Rev. Lett. **78**, 879 (1997).
[28] C. A. Coverdale, C. B. Darrow, C. D. Decker, W. B. Mori, K.-C. Tzeng, K. A. Marsh, C. E. Clayton, and C. Joshi, Phys. Rev. Lett. **74**, 4659 (1995).
[29] V. Malka, E. De Wispelaere, J. R. Marques, R. Bonadio, F. Amiranoff, F. Blasco, C. Stenz, Ph. Mounaix, G. Grillon, and E. Nibbering, Phys. Plasmas **3**, 1682 (1996).
[30] A. Modena, Z. Najmudin, A. E. Dangor, C. E. Clayton, K. A. Marsh, C. Joshi, V. Malka, C. B. Darrow, C. Danson, D. Neely, and F. N. Walsh, Nature (London) **377**, 606 (1995).
[31] D. Umstadter, S.-Y. Chen, A. Maksimchuk, G. Mourou, and R. Wagner, Science **273**, 472 (1996).
[32] Carl Zeiss Geschäftsbereich Sondertechnik, Verterieb Optische Komponenten, 73446 Oberkochen, Germany.
[33] Y. M. Li and R. Fedosejevs, Meas. Sci. Technol. **5**, 1197 (1994).
[34] A. McPherson *et al.*, Nature (London) **370**, 631 (1994).
[35] T. D. Donnelly *et al.*, Phys. Rev. Lett. **76**, 2472 (1996).
[36] D. R. Miller, in *Atomic and Molecular Beam Methods*, edited by G. Scoles (Oxford University Press, Oxford, 1988), Vol. 1.
[37] P. Sprangle, E. Esarey, and A. Ting, Phys. Rev. A **41**, 4463 (1990).
[38] P. Sprangle, E. Esarey, and A. Ting, Phys. Rev. Lett. **64**, 2011 (1990).
[39] P. Sprangle, E. Esarey, and J. Krall, Phys. Plasmas **3**, 2183 (1996).
[40] P. K. Tien, J. P. Gordon, and J. R. Whinnery, Proc. IEEE **53**, 129 (1965).
[41] Y. R. Shen, *The Principles of Non-linear Optics* (Wiley, New York, 1984), Chap. 17.

[42] P. Gibbon, P. Monot, T. August, and G. Mainfray, Phys. Plasmas **2**, 1305 (1995).

[43] *Handbook of Chemistry and Physics* (CRC Press, Cleveland, OH, 1974).

[44] T. A. Carlson, C. W. Nestor, Jr., N. Wasserman, and J. D. McDowell, At. Data **2**, 63 (1970).

[45] B. E. A. Saleh and M. C. Teich, *Fundamental of Photonics* (Wiley, New York, 1994).

[46] A. Sullivan, H. Hamster, S. P. Gordon, and R. W. Falcone, Opt. Lett. **19**, 1544 (1994).

[47] A. J. Mckinnon, M. Borghesi, A. Iwase, M. W. Jones, G. J. Pert, S. Rae, K. Burnett, and O. Willi, Phys. Rev. Lett. **76**, 1473 (1996).

[48] J. Denavit and D. W. Phillion, Phys. Plasmas **1**, 1971 (1994).

[49] W. L. Kruer, *The Physics of Laser Plasma Interactions* (Addison-Wesley, Redwood, CA, 1988).

[50] M. D. Perry, C. Darrow, C. Coverdale, and J. K. Crane, Opt. Lett. **17**, 523 (1992).

[51] P. B. Corkum, N. H. Burnett, and F. Brunnel, Phys. Rev. Lett. **62**, 1259 (1989).

[52] C. B. Darrow, C. Coverdale, M. D. Perry, W. B. Mori, C. Clayton, K. Marsh, and C. Joshi, Phys. Rev. Lett. **69**, 442 (1992).

[53] C. Rousseaux, G. Malka, , F. Amiranoff, S. D. Baton, and Ph. Mounaix, Phys. Rev. Lett. **74**, 4655 (1995).

[54] X. F. Wang *et al.* (unpublished).

[55] C. A. Coverdale, C. B. Darrow, C. D. Decker, N. M. Naumova, T. Zh. Esirkepov, A. S. Sakharov, S. V. Bulanov, W. B. Mori, and K. C. Tzeng, Plasma Phys. Rep. **22**, 617 (1996).

[56] S. C. Rae and K. Burnett, Phys. Rev. A **46**, 1084 (1992).

[57] D. L. Fisher and T. Tajima, Phys. Rev. E **53**, 1844 (1996).

[58] C. D. Decker, W. B. Mori, and T. Katsouleas, Phys. Rev. E **50**, R3338 (1994).

[59] V. P. Silin, Zh. Éksp. Teor. Fiz. **47**, 2254 (1964) [Sov. Phys. JETP **20**, 1510 (1965)].

[60] B. N. Chichkov, S. A. Shumsky, and S. A. Uryupin, Phys. Rev. A **45**, 7475 (1992).

[61] A. Chiron, G. Bonnaud, A. Dulieu, J. L. Miquel, G. Malka, M. Louis-Jacquet, and G. Mainfray, Phys. Plasmas **3**, 1373 (1996).